Title

Tunable, proteolytic dosage control of CRISPR-Cas systems enables precise gene therapy for dosage sensitive disorders

Author List

Noa Katz[1#], Connie An[1#], Yu-Ju Lee[2,3], Josh Tycko[4], Meng Zhang[1], Jeewoo Kang[5], Lacramioara Bintu[6], Michael C Bassik[4], Wei-Hsiang Huang[2,3], Xiaojing J Gao[1,7,8,9*]

[1] Department of Chemical Engineering, Stanford University, Stanford, CA, USA
[2] Department of Neurology & Neurosurgery, Centre for Research in Neuroscience, McGill University, Montréal, QC H3G 1A3, Canada
[3] Brain Repair and Integrative Neuroscience Program, The Research Institute of the McGill University Health Centre, Montréal, QC H3G 1A3, Canada
[4] Department of Genetics, Stanford University, Stanford, CA 94305, USA
[5] Neurosciences Interdepartmental Program, Stanford University, Stanford, CA, 94305, USA
[6] Department of Bioengineering, Stanford University, Stanford, CA, USA
[7] Stanford Bio-X, Stanford University; Stanford, 94305, USA
[8] ChEM-H Chemistry/Biology Interface Training Program, Stanford University, Stanford, CA, USA
[9] Lead contact
*Correspondence: xjgao@stanford.edu
# These authors contributed equally to this work

Summary

The ability to modulate gene expression through modular and universal genetic tools like CRISPR-Cas has greatly advanced gene therapy for therapeutics and basic science. Yet, the inherent stochasticity of delivery methods cause variation in target gene expression at the single-cell level, limiting their applicability in systems that require more precise expression. Thus, we implement a modular incoherent feedforward loop based on proteolytic cleavage of Cas to reduce gene expression variability against the variability of vector delivery. We target a genome-integrated marker and demonstrate dosage control of gene activation and repression, post-delivery tuning, and RNA-based compatibility of the system. To illustrate therapeutic relevance, we target the gene *RAI1*, the haploinsufficiency and triplosensitivity of which cause two autism-related syndromes. We demonstrate dosage-controlled gene activation for both human and mouse *Rai1* via viral delivery to patient-derived cell lines and mouse cortical neurons. Overall, we established a robust dosage control circuit for uniform gene expression, beneficial for basic and translational research.

Introduction

For basic research and potential therapies, it is now routine to deliver genetic materials into cells to change the expression level of target genes using vectors such as lentiviral vectors, adeno-associated virus (AAV), and messenger RNA (mRNA) encapsulated in lipid nanoparticles. Gene regulation can be done directly through delivery of a gene of interest or through tools that can regulate intrinsic gene expression, such as the Clustered Regularly Interspaced Short Palindromic Repeats (CRISPR)-Cas systems, which have been widely adopted due to their modularity and potential to regulate any gene. However, cargo expression stemming from such delivery methods have remained inherently variable, both between individual cells within an experiment and across different experiments.

For basic research, quantitatively maintaining target gene expression at predefined levels against delivery variability would greatly improve our ability to quantitative genotype-phenotype relations, especially when such relations are non-monotonic.[1] In addition, such methods would empower large swaths of biomedical applications sensitive to gene dosage. For example, unnaturally high gene expression can cause unexpected phenotypes and toxicities, compromising the safety and efficacy of potential gene therapies.[2–4] This sensitivity is even stronger in dosage-sensitive genetic disorders, where increased or decreased levels of a gene are both pathological, such as in autism spectrum and neurodevelopmental disorders.[5–7] *RAI1* (retinoic acid-induced 1) is a notable example: its heterozygous loss of function causes Smith-Magenis syndrome (SMS) and its duplication causes Potocki-Lupski syndrome (PTLS).[8–12] SMS and PTLS patients have distinct phenotypes, but both display developmental delays, intellectual disability, and are generally reliant on caregivers into adulthood.[10,13] Current strategies for potential treatment of SMS focus on CRISPR activation (CRISPRa) of the single remaining *Rai1* copy. Direct delivery is not possible, as Rai1 spans 7.6kb, exceeding the packaging limit of AAVs.[14] A similar approach can be taken for PTLS, which is caused by overexpression of *RAI1*, making it suitable for gene silencing via CRISPR-Cas13, a method for targeted RNA knockdown.[15] However, high dosages of either CRISPR systems may lead to overcorrection in some neurons and phenotypes characteristic of the opposing disorder.

Although it is intuitive to reduce the total vector amount delivered to avoid overdosing, this approach can reduce treatment efficacy and does not fully address the underlying stochasticity of gene delivery. First, decreasing the number of viruses will reduce overall coverage, leaving more target cells untreated. Furthermore, delivery methods are inherently inhomogeneous. Systemic infusion of AAVs leads to uneven biodistribution across various organs, and injection of AAVs naturally causes a dosage gradient.[16] Lastly, the process of gene delivery is fundamentally stochastic. In the context of gene therapy, there will be variability in transgene expression across different cells within an individual and from patient to patient.[17,18] We would meet all these experimental and therapeutic challenges if we could bridge the critical gap between the variability of vector delivery and the need for controlling the dosage of the target gene (**Fig. 1A**).

The incoherent feedforward loop (IFFL) is a circuit motif broadly found in natural biological pathways.[19,20] In an IFFL, one common input passes through an activating arm that increases the level/activity of a target gene and a parallel inhibitory arm that decreases it (**Fig. 1B**). These antagonistic arms maintain the output level against input variability: variation in the input will proportionately drive both antagonistic arms, compensating for changes and leading to a steady output level. In the context of gene delivery, the input is dosage or transgene copy number, and the output is transgene expression. In general, an engineered IFFL would ideally (1) depend minimally on the host cell and function robustly across cell types, (2) be compatible with various delivery methods, (3) allow for tuning of transgene expression level pre- and post-delivery, and (4) control the activation and inhibition of diverse target genes.

Previously engineered IFFLs directly or indirectly target a delivered gene using various inhibition factors such as transcriptional repressors, antagonists, and RNAi.[21–29] While all have achieved impressive dosage control, the most prominent mechanism of repression remains RNAi, which has been proven effective in multiple scenarios.. However, there are several limitations to this strategy. First, inhibition of the transgene via miRNA requires endogenous RNAi machinery which leads to variable IFFL performance across cell types.[27,30] Furthermore, RNAi machinery can become saturated at high dosages, compromising the dosage-controlled behavior of the circuit.[23,27,30] Second, for such IFFLs to operate as intended, the components constituting both arms must be constantly produced from the vector. This precludes the use of mRNA vectors which emerging as a dominant delivery method for transient gene expression. Since lipid nanoparticles carrying mRNA accumulate in the liver potentially leading to cargo overexpression and toxicity, mRNA therapies may also benefit from dosage control offered by IFFLs.[31] Third, though the transgene expression level can be tuned pre-delivery though the choice of miRNA and the number of binding sites, dynamic post-delivery tuning is nontrivial to build. Since the optimal dosage and the delivery efficiency of a treatment likely differs between patients, post-delivery tuning using small molecules may prove crucial for a gene therapy's success. For example, both the dosage and timing of gene expression is important for neurodevelopment.

To create IFFLs that meet the above criteria, we reason that proteolytic cleavage is a compelling candidate for the inhibitory arm. Viral proteases are ideal due to their short and highly specific cleavage sites which do not cleave endogenous human proteins. This cleavage event will not rely on additional host cell machinery other than transcription and translation which simultaneously drives both the activation and inhibition arm. Furthermore, such post-translational proteolytic cleavage is compatible with mRNA delivery. Lastly, viral protease systems have been extensively engineered and demonstrated for diverse controls, offering variants suitable for both *a priori* and post-delivery tuning protease activity,[32,33] offering variants suitable for both *a priori* and post-delivery tuning of set points.

As for the activation arm, one could potentially engineer any target protein to be controlled by proteolytic cleavage, but that would require *ad hoc* engineering for each new target. Furthermore, almost a third of autosomal human genes predicted to be both haploinsufficient and triplosensitive are too large to fit into an AAV (**Fig. 1C**), arguably the most promising long-term delivery vector for treating such diseases.[34] Therefore, we set out to indirectly regulate the target gene through CRISPR-based mechanisms. This allows us to overcome the length limitation and grants us flexibility in regulation strength. Additionally, we can now create dosage-insensitive inhibition via CRISPR-based RNA-interference systems, such as the RNA-targeting Cas13.[35] This allows us to target triplosensitivity disorders, such as PTLS, where dosage control is impossible to achieve with current IFFL-based methods that rely on the delivery of the target gene.

Here, we combined experimental and computational methods for the novel implementation of IFFLs based on proteolytic cleavage and CRISPR activation/repression. Using transient, genome-integrated, and endogenous target genes, we demonstrated the IFFLs' feasibility, robustness, mRNA compatibility, tunability and capability of both increasing and decreasing target gene expression. As a therapeutically pertinent example, we applied proteolytic IFFLs to the development of CRISPRa gene therapy for the neurodevelopmental disorder SMS, by controlling *RAI1* dosage via various delivery methods and in multiple contexts. We adapted our IFFL to target human *RAI1* and demonstrated dosage control in both HEK293 and SMS patient-derived cells when delivered via lentiviruses. Lastly, we demonstrated that our IFFL offers robust dosage control of *Rai1* and decreases the upper-bound gene expression variability when delivered via AAVs to a murine neuronal cell line and cortical neurons.

Results

Establishing proteolytic IFFLs for gene activation using synthetic reporters

To demonstrate the feasibility of building proteolytic IFFLs to control the dosage of CRISPRa gene activation, we first developed computational models and designed synthetic reporters to characterize circuit behavior. The activation circuit, which controls the activation of an endogenous gene of interest, consists of two components: a protease and a protease repressible CRISPRa unit (**Fig 1D**). We reasoned that we could repress CRISPRa function by placing a protease cut site between its catalytically inactive Cas9 (dCas9) domain and the transcriptional activation domain. Thus, proteolytic cleavage would abolish the transcriptional activation ability of CRISPRa. To qualitatively explore this circuit's behavior, we developed a computational model using Michaelis-Menten kinetics, ordinary differential equations, and parameter values in experimentally grounded regimes (**Fig 1E**). The model indeed predicted that co-delivery of CRISPRa and the protease reduces the range of target gene activation. Furthermore, increasing the amount of protease relative to CRISPRa should lead to stronger dosage control effects, lowering the gene expression.

Next, to experimentally validate the activation circuit, we engineered a widely used CRISPRa system, *Streptococcus pyogenes* dCas9 (spdCas9) fused to the transcriptional activation domain VP64, to be cleavable by tobacco etch virus (TEV) protease. This was done by inserting the TEV cleavage site between the two domains. TEV protease cleaves a short, specific amino acid sequence that is orthogonal to the human proteome, avoiding off-target cleavage in the host cell. To facilitate characterization, we created a HEK293 cell line with a genomically integrated green fluorescent protein (*GFP*) reporter to act as the endogenous target gene. We then transiently transfected plasmids separately encoding all IFFL components (dCas9, TEV, and the *GFP*-targeting gRNA) and an *mCherry* transfection marker into the reporter cell line (**Fig 1F**). Using multiple plasmids facilitates component swapping and stoichiometry titration for initial optimizations.

The first method we used to measure the IFFL's ability to buffer against variability in dosage is to transfect different amounts of the IFFL plasmids and examine the average *GFP* activation, which we term "circuit titration" (**Fig 1G**). As expected, the *GFP* activation in the reporter cell line was diminished with the transfection of TEV compared to the conditions without TEV, indicating dosage control. The second method we used to measure the IFFL's ability to buffer against changes in dosage was to rely on the fact that the uptake of plasmids during transient transfection is highly correlated,[36] meaning that the mCherry fluorescence can serve as a proxy for the amount IFFL components within a cell. This technique is widely used, and it captures a wider range of vector level variability than circuit titration.(Love et al. 2025) Plotting the running average of GFP fluorescence against dosage (mCherry fluorescence) also confirms dosage control (**Fig 1H**). Furthermore, by increasing the amount of TEV plasmid transfected, the GFP activation decreased which was consistent with our model prediction. However, we also observed that GFP intensity decreased at high transfection levels in the presence of TEV. This trend was also observed when analyzing the running averages of the previous circuit titration experiment, suggesting that taking the average of all transfected cells (Fig S1A) would skew the average GFP fluorescence. Thus, to extract the quantities for **Fig 1G**, we only considered cells that are within the monotonic regime (Fig S1B).

We hypothesized that this non-monotonic effect at high dosages may be due to the creation of inactive dCas9 species that bind to *GFP* and outcompete functional species. We were able to recapitulate this behavior in the simulation upon including competitive inhibition (**Fig 1I**). To further verify that this effect was indeed caused by the presence of cleaved dCas9 species, we created a "pre-cleaved" dCas9 construct that is missing the activation domain. Then we transfected both the "pre-cleaved" construct and the active CRISPRa construct into the reporter cell line. As the amount of "pre-cleaved" dCas9 increased, the average GFP expression decreased, indicating competitive binding (Fig S1C).

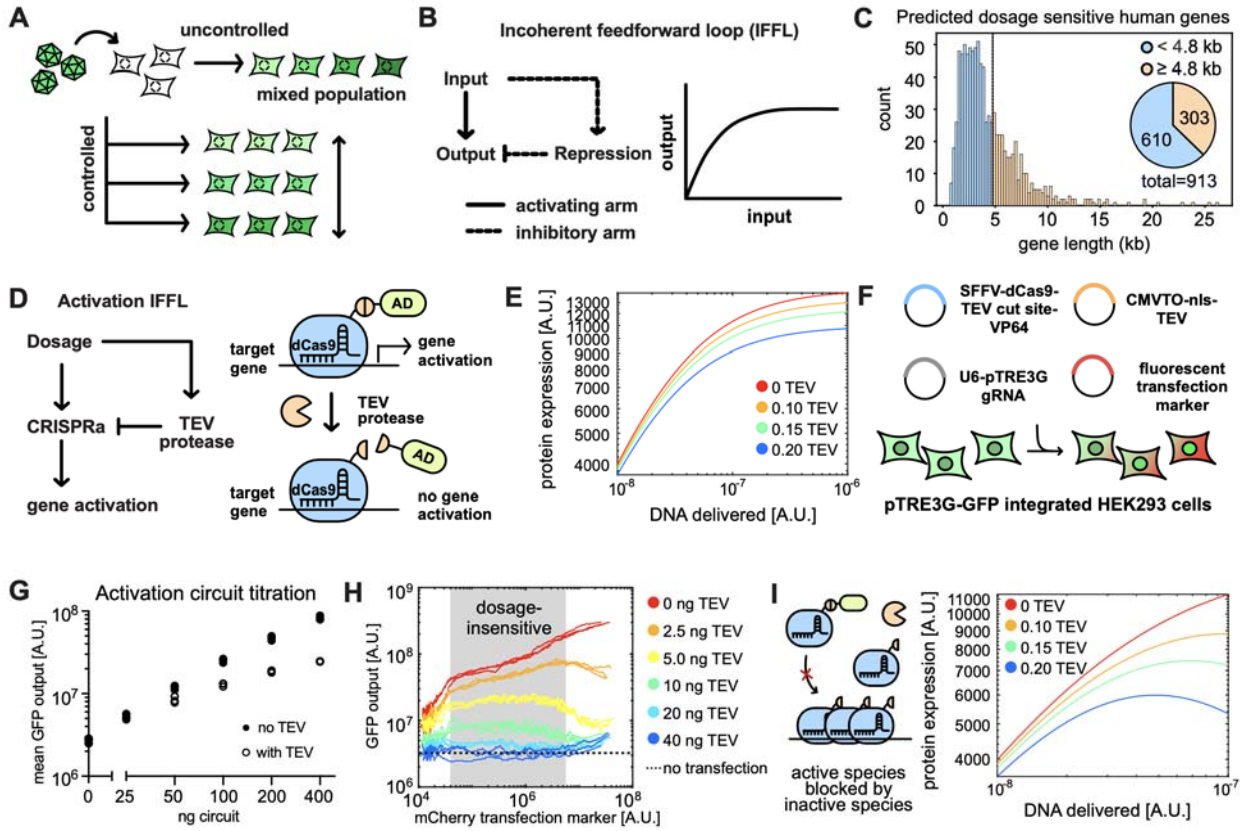

Fig 1 Establishing proteolytic IFFLs for gene activation using synthetic reporters
A Schematic of variable gene expression during gene delivery (uncontrolled) and an ideal gene delivery system which eliminates heterogeneity and tunes gene expression level (controlled).
B Schematic of an incoherent feedforward loop. The input drives two opposing arms which allows the output to remain invariable to the input strength.
C Histogram of sizes of human genes predicted to be dosage sensitive.
D Schematic of engineered activation circuit. TEV protease cleaves off the activation domain (AD) linked to dCas9, creating an IFFL with dosage as the input and CRISPRa activity as the output.
E Simulation of the activation IFFL using ordinary differential equations. TEV fractions represent relative expression.
F Schematic of experimental design for Fig 1G and 1H.
G Dot plot of average GFP fluorescence (output) as a function of circuit transfected in GFP-integrated HEK293 cells.
H Running averages of GFP fluorescence (output) as a function of mCherry fluorescence (transfection marker) as TEV plasmid amount increases.
I Schematic of competitive binding of active and inactive CRISPRa species and simulation of activation IFFL with competitive inhibition.
All experiments shown are based on three independent replicates.

Demonstrating unique features of proteolytic IFFLs

The variation in performance of miRNA based IFFLs is due to the different processes that drive the activation and inhibition arms. The activation arm produces the transgene transcript through transcription while the miRNA is produced through transcription and other processing steps. Though this implementation is effective at producing dosage control, changes in miRNA processing machinery across cell types will affect the strength of the inhibition arm relative to that of the activation arm. (Love et al. 2025; Du et al. 2024) Furthermore, saturation of the RNA-induced silencing complex (RISC), which is necessary for miRNA maturation, can compromise dosage control behavior.(Love et al. 2025; Du et al. 2024) On the other hand, proteolytic IFFLs should perform more robustly across cell types since proteolysis does not rely on endogenous machinery and both arms will be driven by the same processes. To demonstrate this, we genomically integrated a *GFP* reporter gene in Chinese hamster ovary (CHO) cells and COLO320 cells (a colon cancer cell line) like we did for the HEK293 cells in Fig 1F. Transient transfection of the activation IFFL circuit components demonstrated robust dosage control and qualitatively similar performance across all three cell lines (**Fig 2A**).

Another desirable feature of proteolytic IFFLs is their compatibility with mRNA delivery. mRNA vectors have recently emerged as a safer, transient method of transgene expression. We produced *in vitro* transcribed mRNAs separately encoding the CRISPRa components, TEV, and a blue fluorescent protein (*BFP*) transfection marker. Since expression from mRNA is lower than DNA, we replaced the VP64 activation domain with the stronger activation domain NZF[37] in the CRISPRa construct. Transfecting these components into the *GFP*-integrated cell line led to diminished *GFP* activation in the presence of TEV (**Fig 2B**).

Although gene expression modulation can be achieved by varying the stoichiometry of IFFL components (**Fig 1H**), all components will be delivered on the same construct via viral transduction of a gene therapy to minimize performance variability and production cost. Therefore, the stoichiometry of components will remain the same in this scenario. Therefore, to achieve *a priori* tuning of gene expression level, we instead varied the cleavage efficiency of TEV to tune the strength of the IFFL repression arm. One method to adjust cleavage efficiency is to make the cut site more efficient. We accomplished this by inserting two adjacent TEV cut sites between dCas9 and the activation domain. This construct co-transfected with TEV also demonstrated dosage control but required less protease to repress gene activation (Fig S2A). Alternatively, we can adjust the TEV protease efficiency by truncating either the n-terminus or both termini of the protease. As the protease is truncated, it becomes less efficient, and gene expression increased even when keeping the amount of protease plasmid transfected constant (**Fig 2C**, Fig S2B).

Finally, we demonstrated post-delivery tuning of gene expression using two different strategies and small molecules that control protease activity, a useful feature for fine-tuning or adjusting gene expression level over time. First, we used the small molecule rapalog to reconstitute a split TEV protease through dimerization domains fused to each half (**Fig 2D**).[38] Since we predicted that splitting TEV would weaken the repression arm of the IFFL, we used the dual cut site design to improve TEV sensitivity. By increasing the amount of rapalog in the media before transfection of the components, gene activation was reduced (**Fig 2D**). The second strategy used the FDA-approved hepatitis C virus protease (HCVP) small molecule inhibitor Voxilaprevir to tune CRISPRa activity.[39] This involved swapping the TEV cut site between dCas9 and the transcriptional activator for the HCVP cut site. After verifying that HCVP could control the dosage of the modified CRISPRa construct (Fig S2C), we demonstrated that increasing the concentration of Voxilaprevir in the media increased gene activation through repressing HCVP activity (**Fig 2E**).

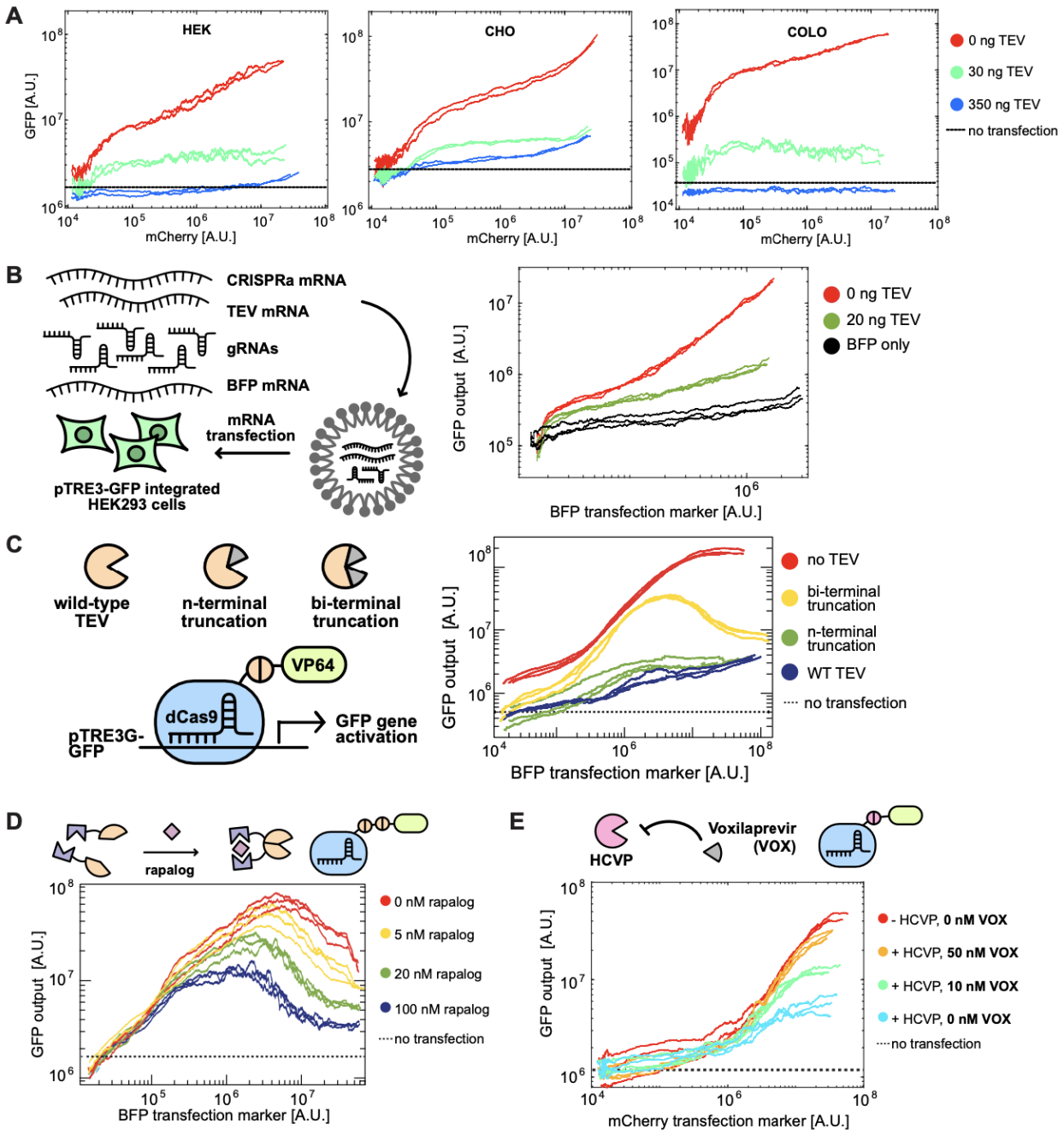

Fig 2 Unique features of proteolytic IFFLs

A Running average of GFP fluorescence (output) as a function of mCherry fluorescence (transfection marker) upon transient transfection of activation IFFL across three GFP-integrated cell lines.

B Schematic of mRNA transfection of activation circuit (left) and running average of GFP fluorescence (output) as a function of BFP fluorescence (transfection marker) upon transient mRNA transfection of IFFL a GFP-integrated HEK293 cell line (right).

C Running average of GFP fluorescence (output) as a function of mCherry fluorescence (transfection marker) upon transient transfection of IFFL using truncated variants of TEV in a GFP-integrated HEK293 cell line. Increasing amounts of truncation reduce cleavage efficiency.

D Schematic of the small molecule rapalog reconstituting split TEV. Running average of GFP fluorescence (output) as a function of mCherry fluorescence (transfection marker) upon transient transfection of IFFL using a rapalog-induced TEV and a double TEV cut site in a GFP-integrated HEK293 cell line.
E Schematic of small molecule Voxiloprevir inhibiting HCVP. Running average of GFP fluorescence (output) as a function of mCherry fluorescence (transfection marker) upon transient transfection of IFFL using HCVP and the HCVP cut site in a GFP-integrated HEK293 cell line.

Establishing proteolytic IFFLs for gene repression using synthetic reporters

Next, we designed a proteolytic IFFL to control the level of gene repression using CRISPR-Cas13 with simulations and synthetic reporters. Like the activation circuit, the repression circuit consists of two components: TEV protease and a TEV-repressible CRISPR-Cas13 (**Fig 3A**). Computational simulation suggests that such an IFFL would achieve dosage control of the down regulation of a target gene (**Fig 3B**). To implement our IFFL, we chose RfxCas13d (CasRx), due to its small size and interest for therapeutic use.[40] Since it has recently been determined that CasRx has strong collateral activity that only occurs when targeting abundant mRNA transcripts,[41] we chose a regime where collateral activity is minimized for experimentation by adjusting the amount of target plasmid and the promoter driving the target gene (Fig S3A).

To establish proteolytic inhibition of Cas13, we screened for cleavage site positions that minimally disrupts Cas13 activity but makes the enzyme susceptible to protease cleavage. We chose candidate sites by examining the AlphaFold predicted structure of CasRx and inserting TEV cleavage sites within the flexible loops (Fig S3B). A previously reported *mCherry* gRNA was used to assess Cas13's on-target cleavage.(Xu et al. 2021) Transfection of *mCherry*, the cleavable CasRx candidates, and TEV allowed us to isolate a variant that maintained the most RNA cleavage activity (**Fig 3C**). However, this displayed limited inhibition by TEV likely due to remaining affinity between the two halves. To improve TEV repression, we added a masked degron to the N terminus based on the based on the "N-end rule".[42] TEV cleavage exposes the degron which serves as a degradation signal for the cell, further reducing Cas13 activity. This strategy improved the repressibility of Cas13 by TEV (**Fig 3D**).

Finally, we performed a circuit titration to demonstrate the ability of TEV and the engineered Cas13 to control the repression of a transfected *mCherry* gene. Here, we titrated the amount of repression circuit (Cas13 and TEV) co-transfected with a constant amount of *mCherry* (target) and *BFP* (co-transfection marker) (**Fig 3E**). Note that the target is co-transfected rather than endogenous. To assess the effects of increasing amounts of circuit on *mCherry* expression, we gated on a cell population with the same transfection level (**Fig 3F**, left and middle panels). This gating ensures that all conditions have comparable amounts of target plasmid as the amount of circuit is titrated. We chose the highly transfected population which has the greatest difference in repression strength due to the amount of circuit delivered. **Fig 3F** (right) demonstrates that with TEV, there was a reduction in *mCherry* repression at high transfection levels compared to without TEV, indicating dosage control.

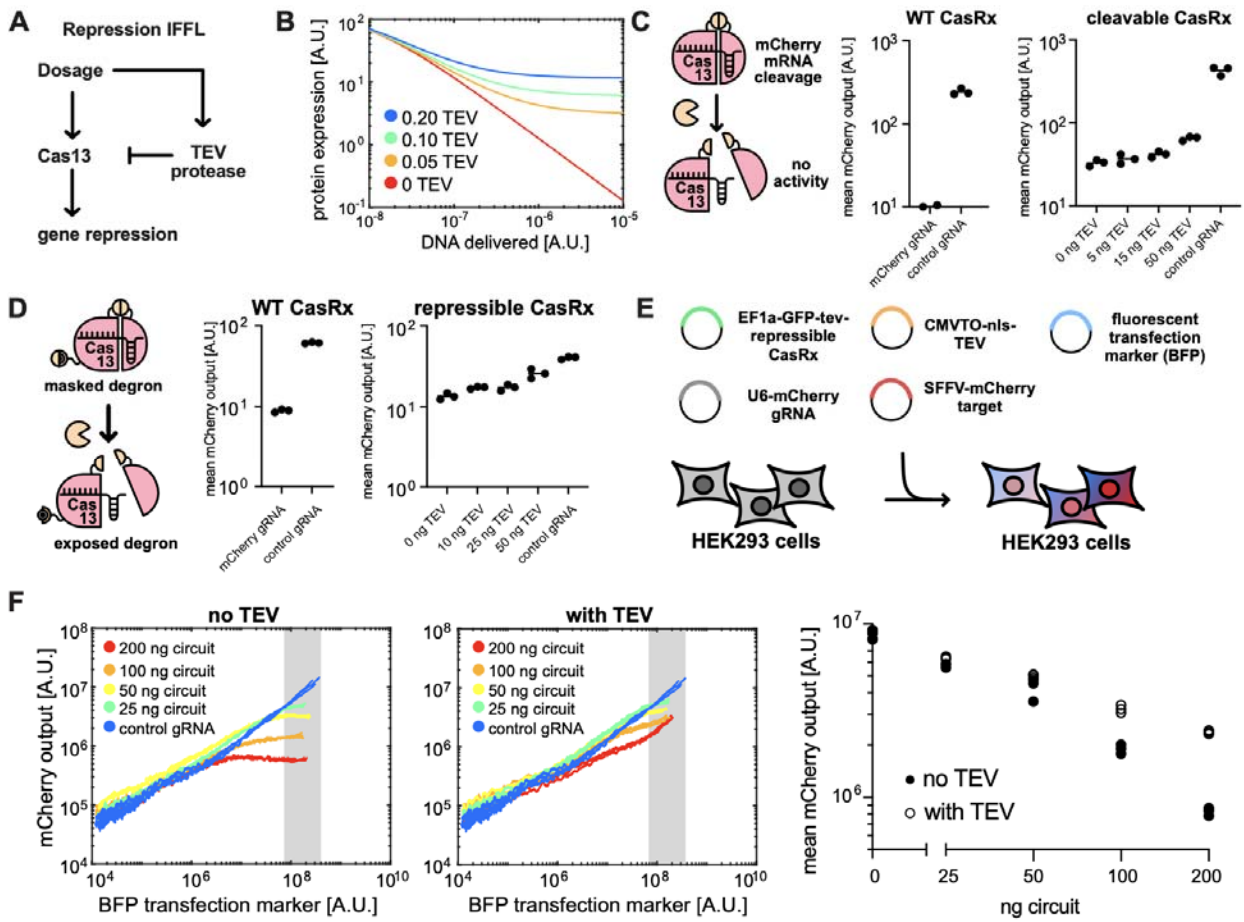

Fig 3 Establishing proteolytic IFFLs controlling gene repression using synthetic reporters
A Schematic of engineered repression circuit. TEV protease inhibits Cas13 through proteolysis, creating an IFFL with dosage as the input and Cas13 activity as the output.
B Simulation of the repression IFFL using ordinary differential equations. TEV fractions represent relative expression.
C Schematic of initial TEV-repressible Cas13 design (left). TEV inhibits CasRx by cleaving the enzyme itself. Dot plot of WT ability to repress expression of a co-transfected mCherry target plasmid (middle). Dot plot of cleavable CasRx ability to repress expression of a co-transfected mCherry target plasmid as the amount of co-transfected TEV plasmid increases (right).
D Schematic of improved TEV-repressible Cas13 design (left). TEV inhibits CasRx by cleaving the enzyme itself and exposing a masked degron, increasing the degradation rate of CasRx. Dot plot of WT ability to repress expression of a co-transfected mCherry target plasmid (middle). Dot plot of cleavable CasRx ability to repress expression of a co-transfected mCherry target plasmid as the amount of co-transfected TEV plasmid increases (right).
E Schematic of experimental design for whole repression circuit titration (Fig 2F).
F Running averages of mCherry fluorescence (output) as a function of BFP transfection marker (left two panels) for whole circuit titration experiment (Fig 2E). Corresponding dot plot of average mCherry fluorescence as a function of circuit transfected (right panel) for highly transfected cells (gray area in left two panels).

Dosage-controlled activation of human *RAI1*

While synthetic reporters facilitate initial optimization, they do not fully represent the challenges one might encounter in actual applications. Using *RAI1* as an example, we set out to examine whether proteolytic IFFLs can achieve dosage control for a therapeutically relevant endogenous gene in a more therapeutically relevant context. Here, we investigate whether the activation circuit can activate *RAI1* in a Smith-Magenis Syndrome (SMS) (*RAI1* haploinsufficiency) human patient-derived cell line to an intermediate level without overshooting into the potentially detrimental PTLS regime (*RAI1* triplosensitivity).

First, we screened for human *RAI1*-targeting guide RNAs in HEK cells and identified one that enabled CRISPR activation of endogenous *RAI1* (Fig S4A). Next, we transfected our IFFL using this gRNA and validated that TEV represses endogenous *RAI1* activation using RT-qPCR. Though the *RAI1* expression determined using RT-qPCR is an ensemble measurement of all cells with varying transfection efficiencies, we demonstrated that increasing TEV expression further repress the activity of CRISPRa (**Fig 4A**).

To reduce variation in circuit performance, we then switched to encoding all IFFL components on a single lentivirus vector, maintaining a strict stoichiometry between CRISPRa, TEV, and the gRNA (**Fig 4B**). As demonstrated in Fig 2C, changing the efficiency of TEV can tune gene activation without altering the stoichiometry of components. We demonstrate this effect on controlling *RAI1* expression by transducing our lentiviral IFFL circuit in HEK cells. To quantify *RAI1* expression at the single cell level, we adopted hybridization chain reaction (HCR) RNA-FISH which quantitatively correlates target RNA expression with fluorescence.[44] shown in **Fig 4D**, we observed IFFL-mediated dosage control of *RAI1* activation. Furthermore, the maximum *RAI1* expression can be tuned by using truncated variants of TEV. We note that the activation range and tunability of *RAI1* via lentiviral transduction is much smaller than the activation of a synthetic gene during transient transfection which is expected due the significantly smaller variability and absolute gene copy number delivered via transduction. The relatively modest variability here is more pertinent to the intended use case where there would be a critical difference between two versus three copies of a causal gene underlying a genetic disorder. Nevertheless, it is promising that the dosage control behavior and tunability of our IFFL hold true when examined over orders of magnitude as well as merely several folds.

Finally, we used a model system to evaluate circuit performance in a human SMS context. We chose patient-derived B-lymphoblastoid cell lines (B-LCLs) which have been used to assess the potential immune phenotype of *RAI1* haploinsufficiency compared to cells derived from healthy individuals.[45] SMS patient-derived LCLs enable us to quantitatively evaluate circuit performance on the only intact copy of *RAI1*. We compared the *RAI1* activation the CRISPRa and IFFL transduced B-LCLs compared to non-transduced LCLs. As can be observed in **Fig 4E**, CRISPRa alone increases *RAI1* mRNA levels by almost threefold, whereas the IFFL brings it back down to around twofold, indicating the functionality of proteolytic inhibition. Most notably, the CRISPRa condition exhibited a long tail of highly activated cells, whereas this tail is less populated or absent in the IFFL conditions. This data indicates that the IFFL reduces upper-bound variability of *RAI1* activation in SMS patient-derived cell lines when delivered via lentivirus.

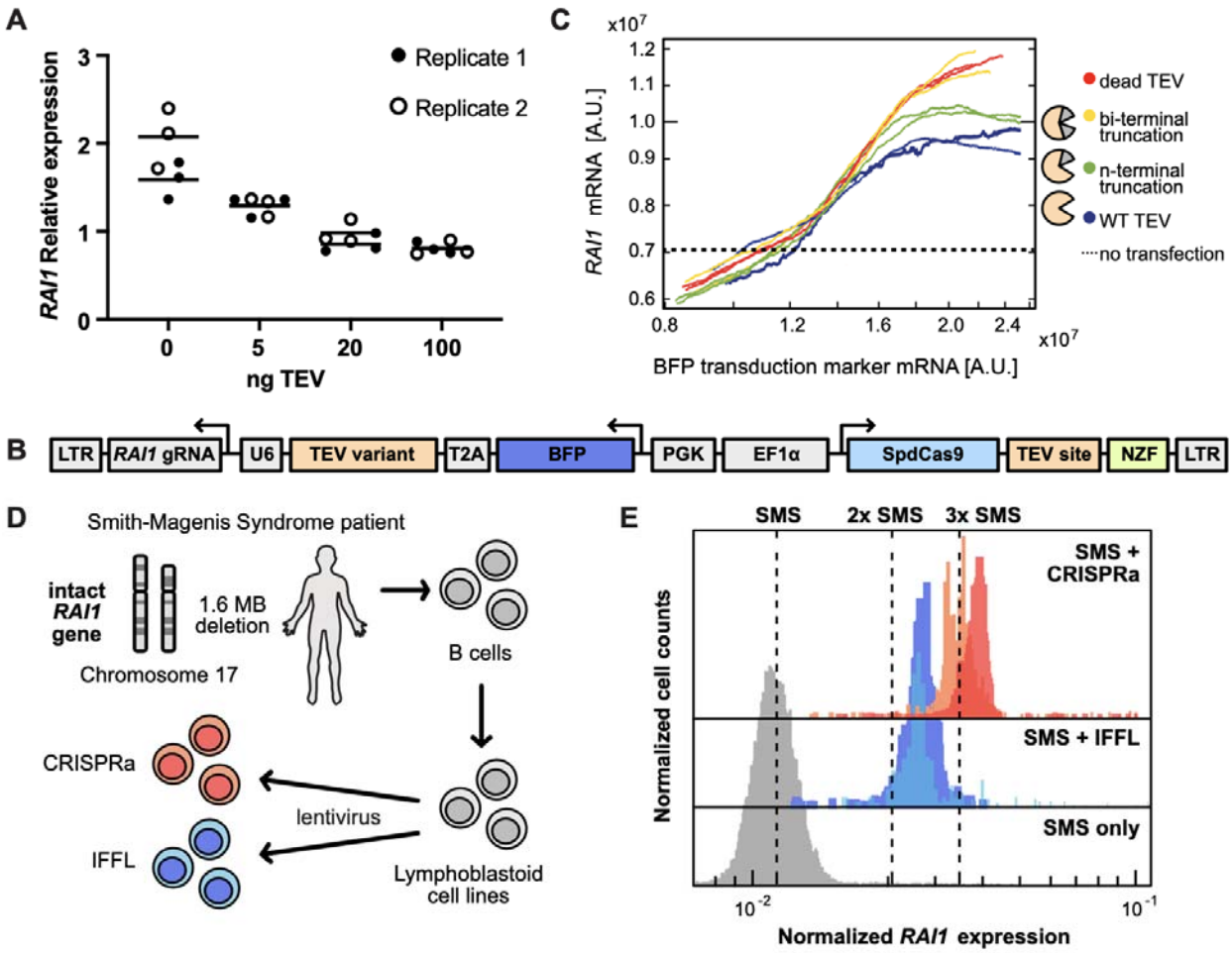

Fig 4 Dosage-controlled activation of *RAI1* in a Smith-Magenis patient cell line
A Dot plot of qPCR results using gRNA targeting RAI1 in transiently transfected HEK293 cells. Results are based on two biological replicates (full and empty circles) and three technical replicates.
B Schematic of lentivirus plasmid design.
C Running medians of RAI1 mRNA as a function of BFP transduction marker mRNA for lentivirus transduction of circuit in HEK293 cells.
D Schematic of patient lymphoblastoid cell line creation and transduction.
E Histograms of normalized *RAI1* expression for each condition of SMS LCLs transduced with the CRISPRa circuit, IFFL, or no transduction. Each color represents an independent replicate. Cells were gated on live SSC-FSC plots, high GAPDH expression, and positive BFP signal. BFP histograms are shown in Fig. S4E. Median levels for CRISPRa, IFFL and SMS-only histograms are 0.365, 0.276, and 0.117, respectively, averaged over the two replicates. CRISPRa and IFFL conditions have two independent replicates with a minimum of 1000 cells in each histogram. SMS-only condition has 90,000 cells.

Dosage-controlled activation of *Rai1* in primary mouse cortical neurons via AAVs

Mouse models of Smith-Magenis Syndrome (SMS) display phenotypes consistent with human SMS and have assisted in determining the timing and brain regions in which restoring *Rai1* expression rescues specific SMS phenotypes.[14,46,47] Recently, AAV-CRISPRa therapy delivered to the paraventricular nucleus of hypothalamus during adolescence was demonstrated to increase *Rai1* expression in an SMS mouse model.[14] This treatment was able to rescue or delay the onset of selective disease features but was not fully curative. It is possible that administering the therapy earlier, increasing the dose, or injecting the whole brain may be able to rescue more phenotypes. We hypothesize that using an IFFL to control the dosage of CRISPRa would allow for increased dosing of the gene therapy without concern of overcorrection. Thus, to prepare for future use of our proteolytic IFFL in an SMS mouse model, we characterized its ability to control the activation of *Rai1* in primary mouse cortical neurons via AAV transduction.

Since, the previous lentiviral design is too large to fit within a single AAV, we shrunk the circuit by combining our previously characterized truncated versions (Fig 2C) with shorter promoters (**Fig 5A**). This design places both CRISPRa and TEV under the regulation of the same promoter. Based on our synthetic characterizations, the amount of CRISPRa required is much higher than that of TEV for successful dosage control. Thus, we reasoned that using the least active and shortest variant of TEV would be sufficient to repress CRISPRa. In addition, we used a minimal U6 promoter to express the gRNA and swapped the 550bp *hSyn* promoter to *pCalm1*,[48] an ultrashort, neuron-specific promoter, to drive both TEV and spdCas9 expression (**Fig 5A**). This construct measures a little below 5 kb between the ITRs, allowing us to produce ample AAVs.

First, we transiently transfected the IFFL and CRISPRa AAV plasmids in N2A cells and quantified *Rai1* activation via RT-qPCR (**Fig 5B**). The CRISPRa condition with a catalytically dead TEV protease showed 7-fold *Rai1* activation, and the IFFL condition with active TEV reduced it to approximately 5-fold. Next, we transduced primary mouse cortical neurons with the AAVs and visualized *Rai1* and *Gapdh* (a housekeeping gene) transcripts using HCR. The *Rai1* transcripts appear as puncta and are more abundant in the CRISPRa and IFFL conditions, indicating robust *Rai1* activation (**Fig 5C**). Most notably, there were visually less *Rai1* transcripts in the IFFL condition compared to the CRISPRa condition. To quantify single-cell *Rai1* expression, we calculated the percent area of each cell that is positive for *Rai1* (**Fig 5D**). Neurons in the CRISPRa condition exhibit much more *Rai1* activation than cells in the IFFL condition. Furthermore, the distribution of *Rai1* expression in the CRISPRa condition is much larger than the IFFL condition which exhibits a truncated right tail.

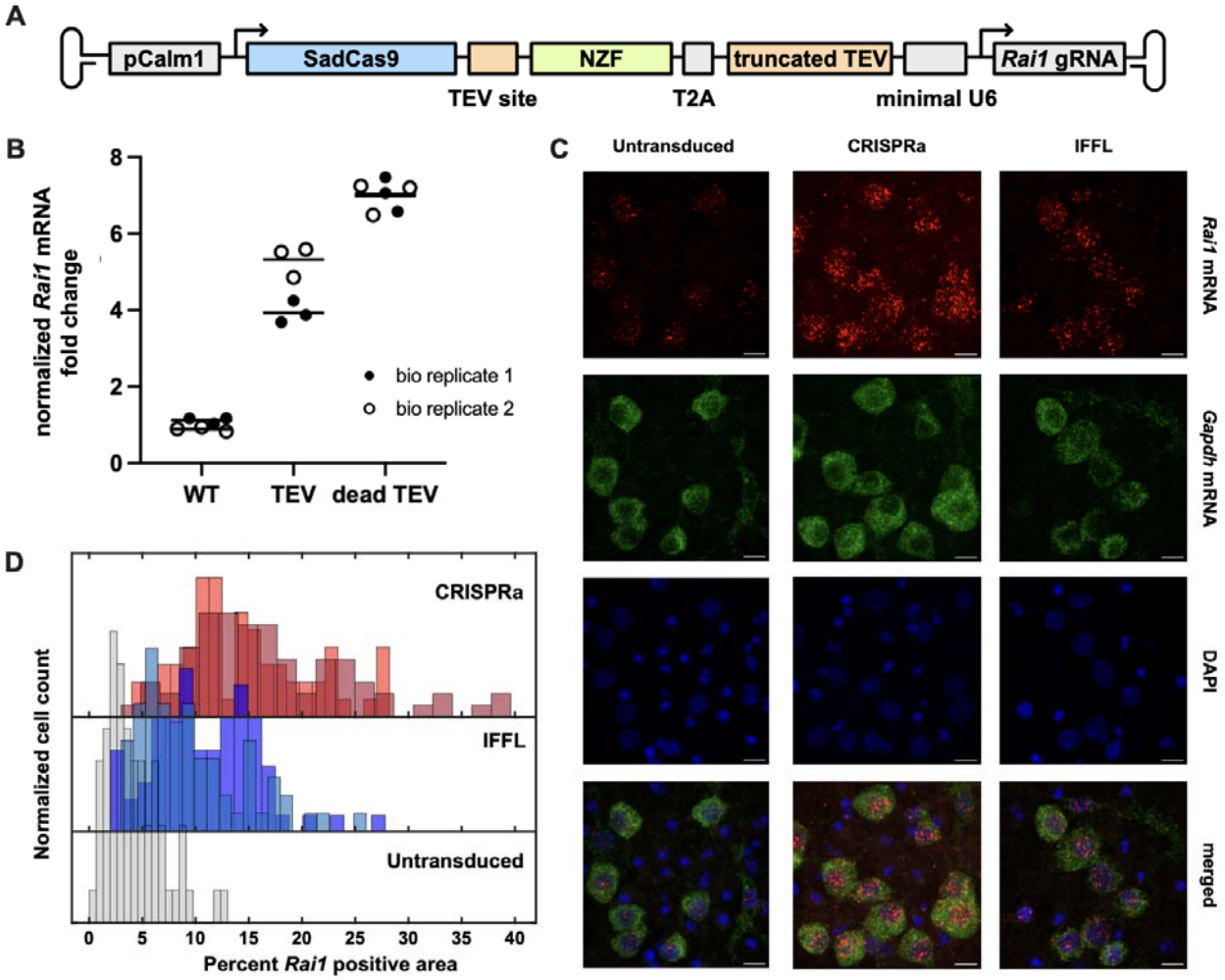

Fig 5 Dosage-controlled activation of *Rai1* in primary mouse cortical neurons using a single AAV
A Schematic of single AAV.
B Dot plot of qPCR results of N2A cells transiently transfected with plasmids encoding the single AAV system. Results are based on two biological replicates (full and empty circles) and three technical replicates.
C Confocal microscopy images of primary mouse cortical neurons transduced with the dual AAV system. *Gapdh* transcripts (AlexaFluor-488), *Rai1* transcripts (AlexaFluor-647), and DAPI were measured using HCR. The range for all *Rai1* channel images was uniformly adjusted to better display *Rai1* mRNA puncta. Scale bars represent 10 µm.
D Histograms depicting the percentage of *Rai1* positive pixels out of total soma region of individual neurons. The untransduced condition contains one replicate with 65 cells. The IFFL and CRISPRa conditions contain two replicates from individual wells each with ~70 cells per condition. Median percent *Rai1* positive areas increased by 2.56-fold (IFFL) and 4.03-fold (CRISPRa) relative to the untransduced condition**.**

Discussion

Scientists have recognized the importance of dosage control via IFFLs for their potential in biomedical applications sensitive to gene dosage as well as their ability to offer better control over gene-manipulation techniques for scientific research. While most successful approaches rely on a delivered gene inhibited by a self-targeting miRNA, we adopted a different strategy. Our IFFL offers a new implementation of IFFL-based dosage-insensitive gene delivery by delivering a protease able to deactivate an engineered CRISPR-Cas system. Guided by our simulations, we first characterized and established the feasibility of this design. Using a synthetic reporter, we observed dosage control of CRISPRa spanning over two orders of magnitude with relatively low amounts of TEV. Our simulation was particularly insightful for understanding the role of competitive inhibition, which can explain the diminishing activation towards very high transfection amounts. We then demonstrated how our protease based IFFL tackles a few fundamental limitations of previous IFFL systems. We established robustness of circuit performance across diverse cell types, mRNA delivery compatibility, and the ability for pre- and post-delivery tuning of gene expression. Utilizing CRISPR-Cas13, we created dosage-controlled gene repression which has not been previously demonstrated. Our approach also grants us compatibility with high-throughput CRISPR-based screens which may benefit from an IFFL's ability eliminate dosage variance between constructs.

Through extensive characterization, we demonstrated how our proteolytic IFFL designs enhance CRISPR-Cas gene therapies by providing improved control over the amount and uniformity of gene regulation at the single-cell level. This is especially relevant for neurodevelopmental disorders which are often caused by deletions or duplications of dosage-sensitive genes. Thus, we demonstrated dosage control of one such gene *RAI1* in both human and mouse contexts. *RAI1* expression requires high precision, as both over-expression and under-expression leads to adverse phenotypes in brain development. We first encoded our entire circuit on lentiviruses to allow for efficient and robust expression in diverse cell types and maintain strict stoichiometry between components. We then demonstrated how the choice of TEV variant tunes *RAI1* expression in HEK293 cells. Lastly, we use an SMS (*RAI1* haploinsufficiency) patient cell line and demonstrated how transduction of our circuit can both activate *RAI1* closer to the two-fold regime than CRISPRa alone and reduce the number of highly expressing cells.

Finally, we demonstrated compatibility of our system with AAV-CRISPRa based therapy in primary mouse cortical neurons, which is the leading gene therapy method for correcting *Rai1* haploinsufficiency in SMS mouse models. To accomplish this, we encoded our circuit on AAVs by minimizing its components while preserving its modularity and universality. We used minimal neuron-specific promoters together with our shortest characterized TEV variant. With the AAVs, we demonstrated that our IFFL reduces upper-bound *Rai1* expression variability while efficiently activating *Rai1* in a controlled manner. Our strategy may potentially alleviate the risk of overcorrection while allowing for higher titers of virus to be used. Ultimately, this study is a milestone in the design and characterization of proteolytic IFFLs and demonstrates their potential role in next-generation CRISPR-Cas gene therapies.

Limitations of the Study

Using our proteolytic IFFL, we demonstrated robust dosage control over CRISPR-Cas activity across various cell types, using different delivery methods, and targeting different genes. Yet, a few aspects of this study require additional work. First, at high transfection levels, we observed a non-monotonic effect in gene activation, likely due to competitive inhibition (**Fig. 1H**). Notably, this behavior is not observed for viral delivery methods, likely because delivered doses are lower. Second, characterization of the repression IFFL would benefit from targeting an endogenous transcript, such as *RAI1*, which is also the cause for the triplosensitive disease PTLS. Third, since our system relies on bacterial and viral sources, it may pose an

immunogenic risk. However, the brain is immune-privileged, meaning that any potential treatment of neurodevelopmental disorders may pose less risk. Furthermore, development of de-immunized tools or using human zinc finger transcriptional activators would improve the safety profile. As for the repression circuit, high-fidelity versions of CasRx can reduce the amount of off-target mRNA cleavage which also improves safety.[43] Lastly, the therapeutic potential of our *Rai1*-targeting IFFL would be best characterized in an SMS mouse model, with the AAVs directly delivered to the relevant brain region. Comparison of disease phenotypes and *Rai1* expression in the brain using HCR in WT, IFFL-, or CRISPRa-treated mice would inform our understanding of circuit performance *in vivo*. Despite current limitations of our system design and depth of study, this work nonetheless pioneers protease based IFFLs and demonstrates their multiple qualitative advantages for both basic and translational research.

Supplementary Figures

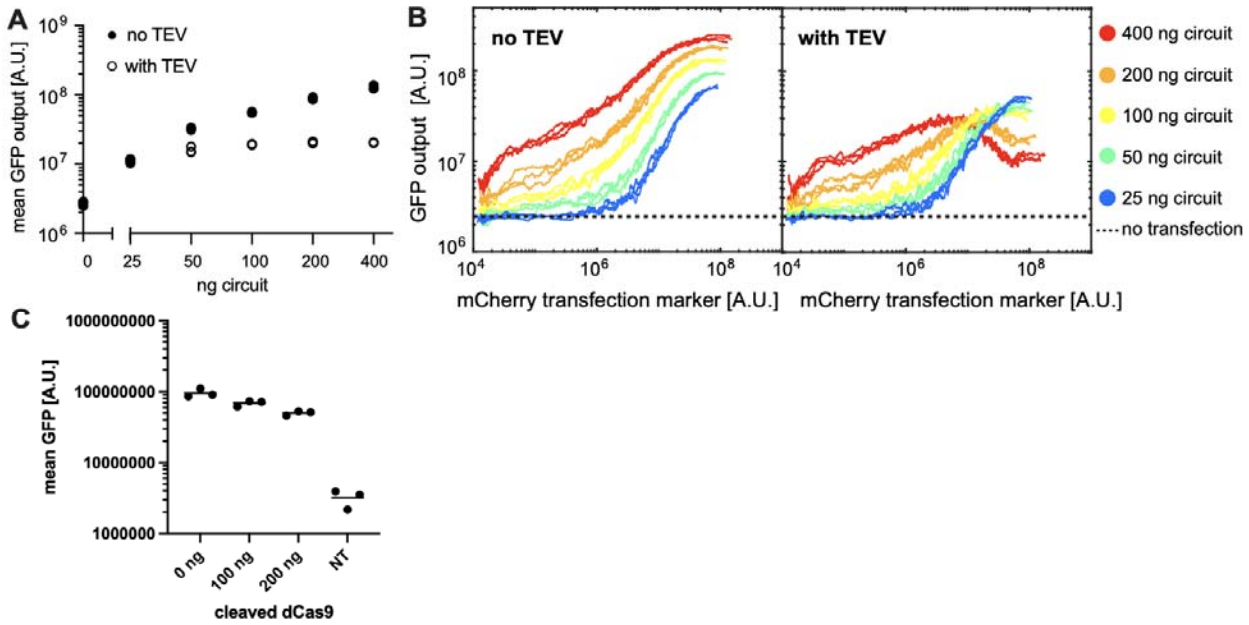

Fig S1

A Dot plot of mean GFP (output) of all transfected cells as a function of circuit transfected in GFP-integrated HEK293 cells.

B Running means of GFP (output) as a function of mCherry transfection marker for activation circuit titration. In highly transfected cells, there is a non-monotonic effect where GFP decreases.

C Dot plot of mean GFP expression as more “pre-cleaved” dCas9 species are transfected along with a constant amount of active dCas9 species.

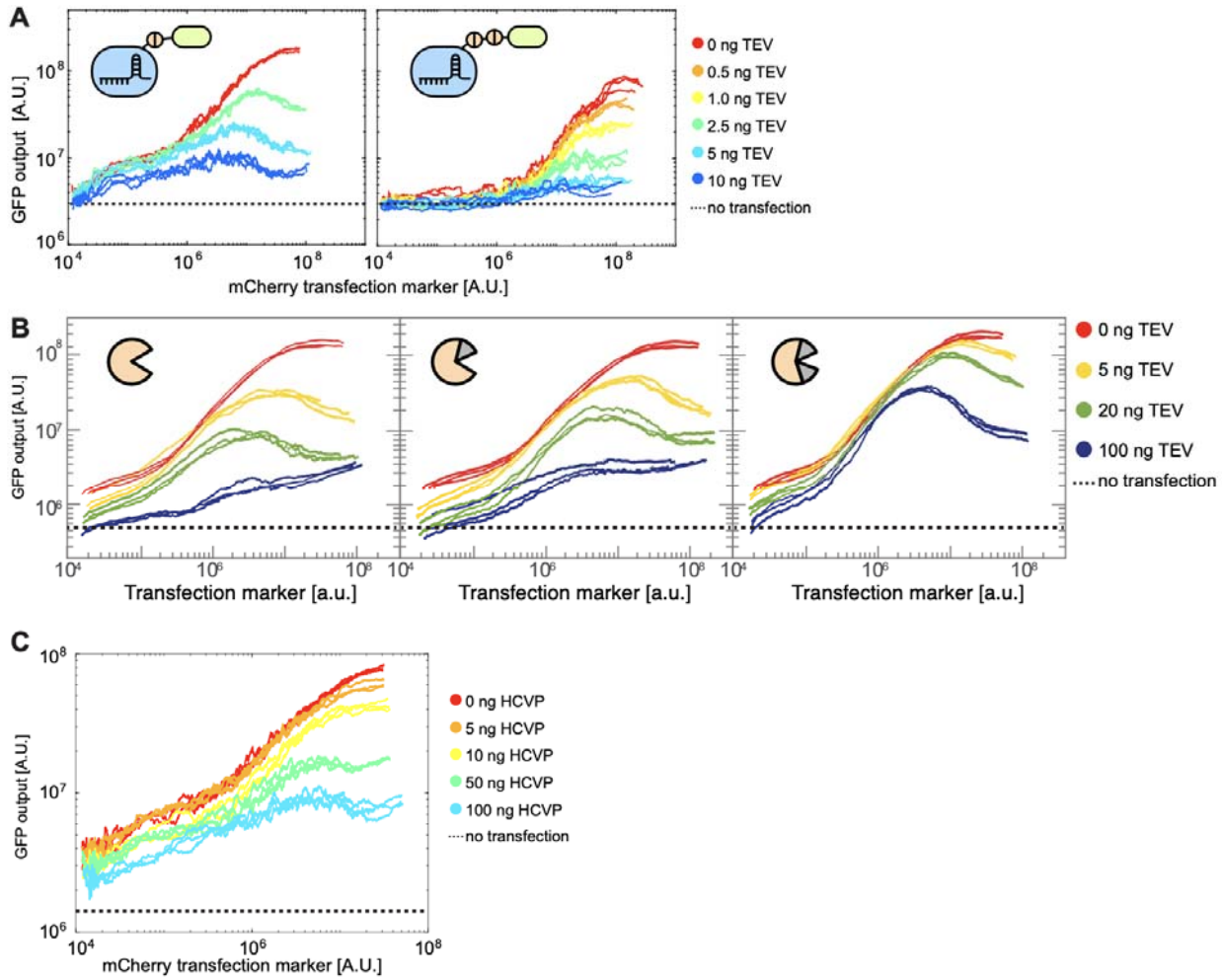

Fig S2

A Running average of GFP fluorescence (output) as a function of mCherry fluorescence (transfection marker) upon transient transfection of IFFL with a single (left) or double (right) TEV cut site in a GFP-integrated HEK293 cell line.

B Running average of GFP fluorescence (output) as a function of mCherry fluorescence (transfection marker) upon transient transfection of IFFL different amounts of TEV variants a GFP-integrated HEK293 cell line.

C Running average of GFP fluorescence (output) as a function of mCherry fluorescence (transfection marker) upon transient transfection of IFFL with HCVP and HCVP cut site in a GFP-integrated HEK293 cell line.

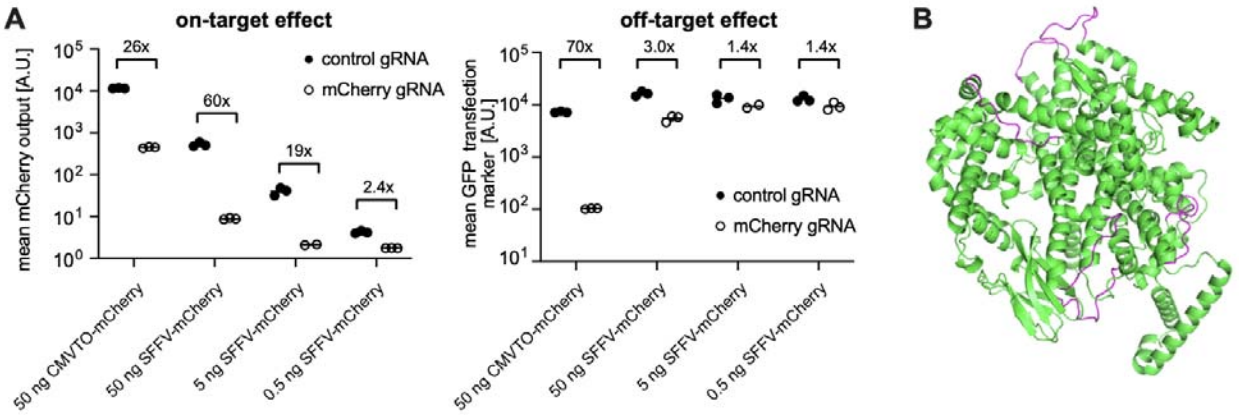

Fig S3

A Dot plot of mCherry fluorescence (left) and GFP fluorescence (right) of WT CasRx transfected with various amounts of target (mCherry) expression. The GFP gene is on the same transcript as CasRx itself. 50 ng of SFFV-mCherry was used in all subsequent experiments.

B AlphaFold structure of CasRx. Candidate flexible loops are magenta.

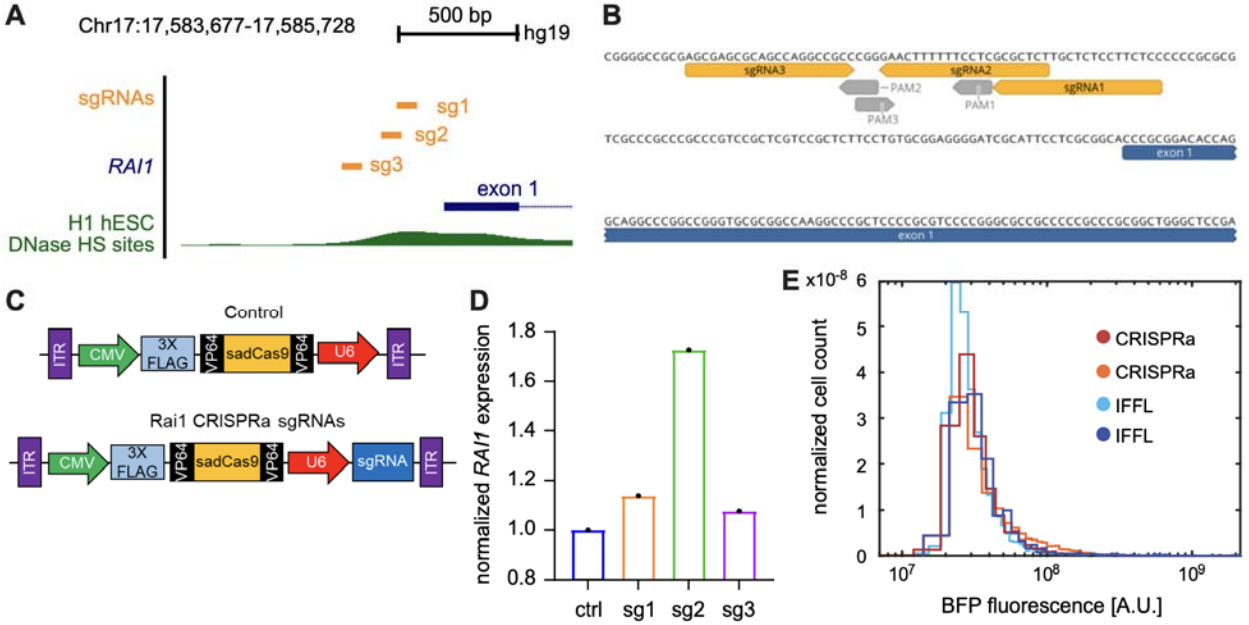

Fig S4

A Identification of a human *RAI1* sgRNA that upregulates *RAI1* expression in 293A cell line. Schematic representation of the positions of sgRNAs (orange) in the human RAI1 promoter. DNase hypersensitive sites (HS) in H1 human embryonic stem cells with open chromatin configurations are shown in green.

B Positions and sequences of three candidate sgRNAs (orange) followed by Sa protospacer adjacent motif (PAM) sequences (gray) within human *RAI1*'s proximal promoter.

C Schematic representation of the sadCas9-2 × VP64 constructs used in gRNA screen.

D Bar plot of qRT-PCR results after sadCas9-2 × VP64-sg2 vector transfection in HEK293 cells.

E Histograms of *BFP* fluorescence for SMS patient B-cells transduced with either CRISPRa or the feedforward circuit.

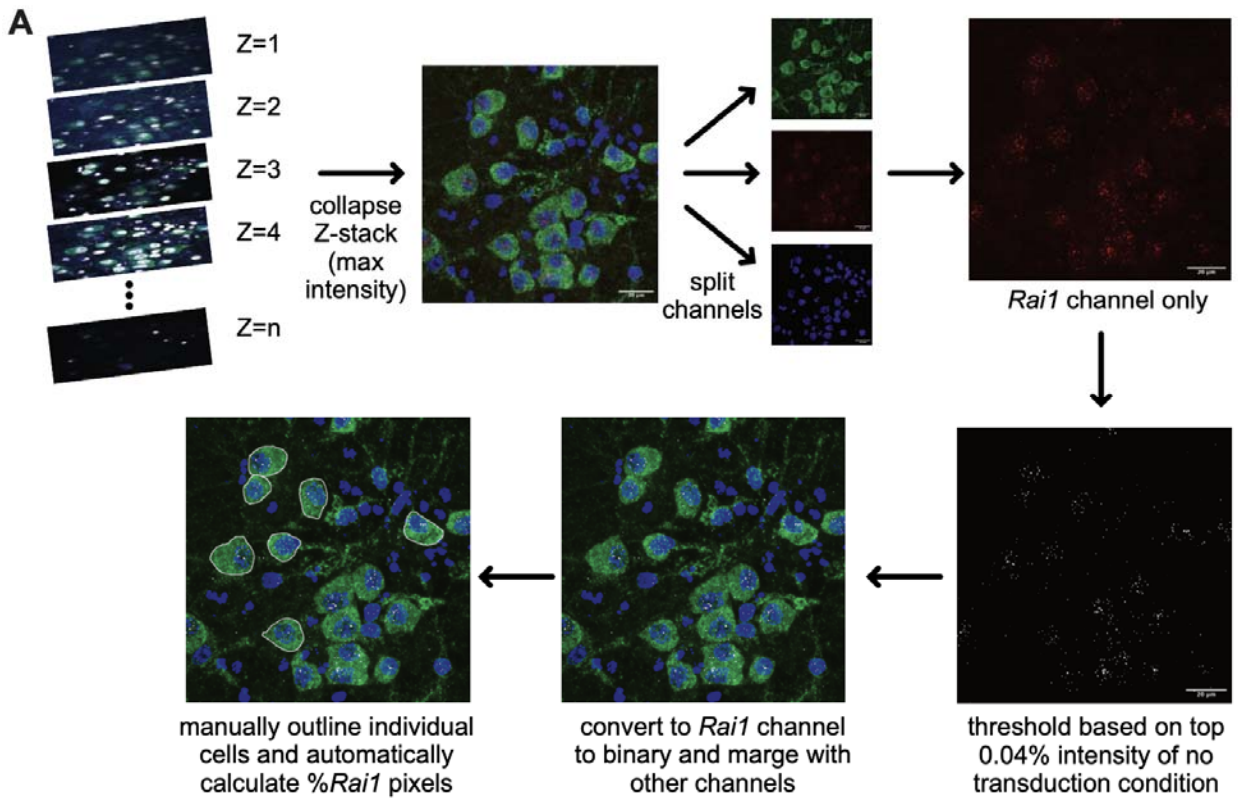

Fig S5

A Schematic of confocal microscopy image processing steps for transduced and untransduced primary mouse cortical neurons.

Acknowledgements
This work was funded by the National Institutes of Health (4R00EB027723-02; to X.J.G.), Simons Foundation Autism Research Initiative - 2021 Genomics of ASD: Pathways to Genetic Therapies (to W.H.H & X.J.G.), Seed Grant from Brain Research Foundation (to X.J.G.), NARSAD Young Investigator Grant from the Brain and Behavior Research Foundation (to X.J.G.), Longevity Impetus Grant (to X.J.G.), Stanford Science Fellows (to N.K.), Fulbright Foundation (to N.K.), N.K. is an Awardee of the Weizmann Institute of Science—Israel National Postdoctoral Award Program for Advancing Women in Science. We thank the Gao lab members for their feedback. We thank C. Liou for technical advice on qPCR and A. Vlahos for technical advice on microscopy analysis.

Author Contributions
N.K., C.A., and X.J.G. designed the study. N.K., C.A., Y.J.L performed and analyzed all the experiments, with support from W.H.H for the RAI1 human gRNA and general Rai1 work, and from J.T, L.B., and M.C.B for the NZF activation domain. M.Z. and J.K. assisted with mRNA synthesis and primary mouse neuron work, respectively. N.K., C.A., and X.J.G. wrote the manuscript with input from all authors.

STAR Methods

Construction of plasmids
Plasmids were generated using standard molecular cloning practices, including the following methods: In-Fusion, ligation, PCR, and annealing. All transgene sequences were ordered from Twist Biosciences or PCR amplified from plasmids (Addgene) using primers ordered from IDT and Thermo Fisher Scientific. Backbone plasmids were restricted using restriction enzymes from Fisher or NEB and purified. Then transgenes and backbones were assembled via in-fusion (Takara) or ligation (NEB), transformed via the heat-shock protocol into competent *E. coli* cells (Turbo-NEB), and plated on carbenicillin containing agar plates. Plasmids were extracted using Qiagen miniprep kits and verified by either Sanger sequencing or whole-plasmid sequencing (Pladmidsaurus). Plasmid sources for dCas9 and TRE-targeting gRNA were generous gifts from Prof. Stanley Qi at Stanford.

Tissue culture
All cells were cultured in a humidity-controlled incubator under standard culture conditions (37°C with 5% CO2).

HEK293, COLO320, N2A, and CHO cells
HEK293 cells (catalog no. CRL-1573), and N2A cells (VWR, catalog no. MSPP-CCL131) were purchased from ATCC while COLO320 cells were a gift from the Howard Chang Lab and cultured using Dulbecco's modified Eagle's medium (Fisher, 501015428) supplemented with 10% fetal bovine serum (FBS) (Fisher Scientific catalog no. FB12999102), 1□mM sodium pyruvate (EMD Millipore catalog no. TMS-005-C), 1% penicillin-streptomycin (Genesee catalog no. 25-512), and non-essential amino acids (Genesee catalog no. 25-536). CHO cells were a gift from the Longzhi Tan Lab and cultured using F-12K nutrient mixture (Fisher, 21127022) supplemented with 10% FBS and 1% penicillin-streptomycin. The GFP-integrated HEK, COLO, and CHO cell lines were cultured in similar conditions with the addition of Hygromycin.

Lymphoblastoid cell lines (LCLs)
LCLs were purchased from the Coriell Institute (catalog no. GM23786) and cultured according to their protocol using RPMI medium supplemented with 10% FBS and 1% penicillin-streptomycin. They were grown in vessels for suspension cells with a breathable film cover. Cells were split once every three days and cultured at a 1:5 ratio in fresh media.

Mouse cortical neurons

Primary mouse neurons were purchased from Thermo Fisher Scientific (catalog no. A15585), thawed, and cultured according to recommended guidelines. Medium was prepared as follows: Complete Neurobasal™ Medium supplemented with GlutaMAX™ -I Supplement (Cat. no. 35050) and B-27™ Supplement (Cat. no. 17504) to final concentrations of 0.5mM and 2%, respectively. Plates were prepared as follows: 24-well plates were incubated with Poly-D-Lysine in PBS at 4.5 µg/cm2 for 2 hours in a biological hood, followed by 3x washes with water. Plates were then left open to dry for 1-2 hours and kept at 4C until use. Cells were thawed and cultured as follows: cells went through rapid thawing (< 2 minutes) of the frozen vial in a 37°C water bath, then transferred to the cell culture hood. Pipette tip was rinsed with complete medium and very gently transferred the cells to the pre-rinsed 50 mL tube 3 mL of complete medium (pre-warmed to 37℃) was added to the cells in the 50 mL tube extremely slowly at the rate of one drop per second. The suspension was then mixed and seeded in a pre-coated glass bottom 24-well plate (ibidi, 82426) with 1ml complete medium pre-warmed to 37°C at 200k cells per well. 50% of the media was changed 24 hours post-seeding and repeated every 2-3 days.

Transient DNA transfections

Cells were cultured in 24-well tissue culture-treated plates under standard culture conditions. When cells were 60–90% confluent, they were transiently transfected with plasmids via the jetOPTIMUS DNA transfection reagent (Polyplus catalog no. 117-15), as per manufacturer's instructions using 0.4 µl of reagent per 50 µl of jetOPTIMUS buffer for 500 ng total DNA transfections in the 24-well plate. To create GFP integrated cell lines, we transfected HEK293/CHO/COLO cells with NK90 piggybac plasmid (pTRE3-GFP) with a matching transposase, let them grow for 72 hours, and then added Hygromycin for selection. After 7 days, surviving cells were frozen and used in all relevant experiments.

mRNA synthesis and transfection

The DNA templates for in vitro transcription contained dCas9 and TEV coding sequences flanked by optimal 5' and 3' UTRs as well as a T7 promoter and PolyA tail (NK409, NK411). The plasmid template with optimal UTRs was a gift from Prof. Michael Elowitz. In vitro transcribed mRNA was produced and purified by GeneScript Inc. based on the DNA template. gRNAs were produced based on Precision gRNA Synthesis Kit (Thermo Fisher Scientific, A29377). The purified mRNAs and gRNA were then transfected to HEK293-pTRE3G-EGFP at 90% confluency via the Mirus TransIT®-mRNA Transfection Kit following the manufacturer's instructions. Briefly, 3 µl of TransIT-mRNA reagent as well as mRNA boost were mixed with mRNA and gRNA per well in 24 well plate. Expression of fluorescent proteins on the mRNA was assayed via flow cytometry 48 hours post transfection.

Flow cytometry and data analysis

Cells were harvested approximately 48 h post transfection by trypsinization and resuspended in flow buffer (HBSS + 2.5 mg ml−1 bovine serum albumin). Cells were analyzed by flow cytometry (Biorad ZE5 Cell Analyzer), and data was processed with Matlab/FlowJo. Cells were gated for live and single cells based on FSC/SSC and FSC-A/FSC-W plots. They were then sorted according to the transfection marker signal and their output fluorescence signal averaged over a running window of 1%-5% of total count. Running averages of output fluorescence were then plotted on as a function of transfection marker signal. For HCR experiments, the fluorescent signal detected was altered to AlexaFluor-488, AlexaFluor-546, and AlexaFluor-647, for detection of GAPDH, BFP and Rai1, respectively.

RNA extractions and quantitative PCR

Cells were grown as detailed above and were spun down at 500g for 5 minutes. RNA was then extracted using RNAasy mini kit (Qiagen), RNase-Free DNase Set (Qiagen), and QIAshredder (Qiagen). After extraction RNA concentration was measured via nanodrop. 3000 ng of purified RNA was then reverse transcribed using SuperScript™ IV First-Strand Synthesis System (Invitrogen). cDNA was then diluted and added to a qPCR compatible 96-well plate (Fisher, 4346907) together with qPCR master mix: SENSIMIX SYBR HI-ROX (VWR, 490017-866 / 868) and primers targeting human or mouse Rai1 gene. qPCR was carried out on a QuantStudio3 (Applied Biosystems) using SYBR-Green. RNA estimation was calculated based on the calibration curve of purified plasmid and normalized by the *Ct* threshold. The following primer pair sequences for mouse Rai1, human Rai1 and normalizing gene (β-actin) were used: Rai1-mouse-F, GCTCGTGACAGCTGGTACA; Rai1-mouse-R, AGGAACACTGGGTCCATGAG; Gapdh-Mouse-F, CATGGCCTTCCGTGTTCCTA; Gapdh-Mouse-R, CCTGCTTCACCACCTTCTTGA; RAI1-human-F, CCCAGGAGCACTGGGTGCATGA; RAI1-human-r, GCAGCTGGAACACATCATGTCCACG; β-actin-human-F, CGTCCACCGCAAATGCTT; β-actin-human-R, GTTTTCTGCGCAAGTTAGGTTTTGT.

dCas9 *RAI1* gRNA screening

The sgRNA oligonucleotides targeting human RAI1 promoter regions were designed using the Benchling gRNA Design Tool.[49] The sadCas9-2 × VP64 vector (Addgene #135338)[50] was used as a backbone vector. It carries mutations in the endonuclease catalytic residues (D10A, N580A) of a FLAG-tagged saCas9, which was fused on both N and C termini with transcriptional activators VP64 (four copies of VP16). sgRNAs were then cloned into the backbone using the ligation cloning method previously described. After validating the sequences of constructs, they were transfected into 293A cells using polyethylenimine, and cells were harvested in TRIzol reagent 72 hours after transfection. Total RNA was extracted using phenol-chloroform extraction method, reverse-transcribed using the SuperScript III First-Strand Synthesis System (Thermo Fisher), and qPCR reactions were conducted using SsoAdvanced Universal SYBR Green Supermix (Bio-Rad) in StepOnePlus real-time PCR system (Applied Biosystems) with GAPDH as a housekeeping control.

The primers used for quantitative PCR were as follows: RAI1-human-F, CCTCAGCATTCCCAGTCCTTC; RAI1-human-R, CTGTGCAACTCTTATAGGAGTGG; GAPDH-human-F, AAGGTGAAGGTCGGAGTCAA; GAPDH-human-R, AATGAAGGGGTCATTGATGG.

CasRx repression work

<u>Determining the minimal collateral activity regime</u>

To facilitate screening of cleavable CasRx designs, we use a synthetic system where we use the fluorescent protein mCherry as the output. Since it has been reported that CasRx can cleave non-target RNA, we first determine the regime in which this collateral activity is minimal. Since collateral activity for CasRx depends on target mRNA level,[41] we titrate mCherry expression level (the target mRNA) by changing the promoter of the mCherry plasmid (CMVTO or SFFV) and the amount of plasmid transfected. We also measure GFP fluorescence which is expressed on the same transcript as CasRx (EF1a-GFP-T2A-CasRx) to determine the amount of off-target effect (SFig. 2A). Transfecting 50 ng of SFFV-mCherry plasmid resulted in the greatest fold change in mean mCherry fluorescence between control gRNA and mCherry-targeting gRNA and minimal difference between mean GFP fluorescence.

Engineering and screening cleavable CasRx variants

Based on the results from the previous section, we transfect 50 ng of SFFV-mCherry, 200 ng of the EF1a-GFP-T2A-CasRx_variant, and 200 ng of the mCherry-targeting gRNA for the following cleavable Cas13 experiments.

To engineer a cleavable CasRx, we first screen for locations within CasRx to place the TEV cut site. Ideally, we would like the cleavable CasRx to (1) have similar mRNA cleaving activity as wild-type CasRx and (2) be inhibited by the presence of TEV. Since there is no crystal structure for CasRx, we use AlphaFold to predict its structure and find flexible loops that we can replace with the TEV cut site or where we can insert the TEV cut site. We screened 8 constructs, and our best candidate was cleav_CasRx7 which had similar mRNA cleaving activity as WT CasRx7 (Fig. S2B). However, there was no appreciable TEV repression of mRNA cleavage activity. To improve the ability of TEV to repress activity of cleav_CasRx7, we added a TEV-cleavable N-end degron to the construct. Degrons are used to regulate degradation rates in cells. In the absence of TEV, the degron is masked. After TEV cleaves the N-end degron, the degron will be exposed, marking the protein for degradation, and decreasing its half-life. Since the N-end degron is appended to the N-terminal of the protein, it should not interfere much with the activity of cleav_CasRx7. Indeed, this construct (teD-cleav_CasRx7) was more TEV sensitive than cleav_CasRx7 and retained its efficiency (Fig. S2C).

Repression circuit titration

Lastly, we used teD-cleav_CasRx7 in a whole circuit titration. We transfect 50 ng of SFFV-mCherry and varying amounts of the teD-cleav_CasRx7 circuit. We use BFP as a transfection marker and average the mCherry fluorescence for cells that are highly transfected (BFP fluorescence > 10^8 A.U.) to produce Fig. 2E. Note that in the running average plots (Fig. S2D), the output mCherry fluorescence increases as dosage increases (BFP transfection marker) which is expected. This is because the mCherry gene is not integrated into the cell's genome and is instead transcribed from a transfected plasmid. Thus, the relationship between mCherry fluorescence and dosage is not the same as in Fig. 2D which is derived from the simulation which assumes that the target gRNA is produced from an integrated gene.

AAV production and transductions

AAVs were ordered and manufactured with the help of the Stanford Gene Vector and Virus Core (GVVC). Plasmids were amplified and extracted via the Qiagen plasmid midiprep kit (Qiagen), their concentration measured and sent to GVVC for production. The AAVs were measured for their ITR as well: NK442: 4.57e13 vg/mL and NK443: 2.70e13 vg/mL. For a 24-well of primary neurons, 4ul of virus was added to the media. Cells were monitored via the EVOS M7000 Cell Imaging System every day and were fixed 2.5 weeks after AAV transduction once a BFP signal was detected (if applicable).

Lentivirus production and transductions

LentiX cells were seeded in 6-well tissue culture plates one day prior to transfections. When cells were 80%-90% confluent, they were transiently transfected with plasmid constructs (600 ng PAX2, pMD2g, and 1,100 ng transgene plasmid) as detailed earlier. Cells were incubated for 24 h under standard culture conditions and were supplemented with 3ml of complete DMEM media to each well. Lentivirus was concentrated 24 hrs afterward using viral precipitation: for each lentiviral prep, media was filtered using a syringe and 0.45 µm filter into 15 mL conical tubes. 5x Lentivirus Precipitation Solution (Alstem 480 catalog no. VC100) was mixed with each prep and incubated at 4 °C for 48-72 hours. Viruses were then spun down at 1500xg for 30 min at 4 °C. Supernatant was aspirated, and virus was resuspended using 200 µL complete media (either DMEM for HEK293 and N2A, or RPMI for LCLs). Virus was then added to cells according to the following protocols, and leftover was frozen at -80°C for further use.

HEK293 and N2A cells
Virus was added dropwise onto 24-well tissue culture plates containing HEK293 or N2A cells seeded at 200k cells/well. Media was changed 24 hours post transduction, and cells were grown for an additional 5 days, at which time a positive BFP signal was detected, and then fixed and stained according to the following protocols.

Lymphoblastoid cell lines (LCLs)
Patient LCLs were split a day prior to transduction at a ⅓ ratio for optimal growth. On the day of transfection, cells were counted and 50k cells were transferred to multiple wells of a 96-well plate. Cells were then spun down at 500xg for 5 min and the media was gently taken out. Virus solutions were then supplemented by Polybrene (Merc) to a final concentration of 10ug/ml, and the mixed solutions were gently added to the cells without resuspension. Cells were then placed in the incubator overnight, and the virus solution removed by centrifugation (500xg for 5min). Cells were then merged and expanded, transferring from 96-well plates to a 48-well plate and finally a 24-well plate. Once cells reached confluency in 24-well plates, they were fixed and stained according to the following protocols.

Cell fixation and Hybridization Chain Reaction (HCR)
DNA probes for GAPDH, RAI1 and BFP were designed and ordered from Molecular Instruments based on the full-length genes with maximal available probe set size of ~7500bp (Fig. 3D+3F and Fig. 4B+4D). Gating was done based on positive probe signals, FSC-SSC for live cells, high GAPDH for active cells, and positive BFP mRNA signal for HCR-flow. All protocols were conducted according to Molecular Instruments HCR protocols. Briefly:

Cells in suspension: HEK293, N2A, B-LCL cells
Day 1: Growth media was aspirated from culture plates and cells were washed with DPBS. Cells were then trypsinized and quenched by the addition of growth media. These steps were omitted for suspension cells (B-LCLs). Cells were then transferred to 15 mL conical tubes and centrifuged for 5 min at 180xg. Cells were then resuspended in 4% formaldehyde to reach approximately 1 million cells/mL. Cells were fixed for 1 hr at room temperature, and then centrifuged and washed with PBST 4 times. Cells were then re-suspended in cold 70% ethanol overnight.
Day 2: Cells were centrifuged for 5 min and washed twice with 500 µL of PBST. PBST was then removed, and the pellets were resuspended with 400 µL of probe hybridization buffer and pre-hybridized for 30 min at 37°C. In the meantime, probe solution was prepared by adding a fixed amount of each probe set to 100 µL of probe hybridization buffer pre-heated to 37°C. Amounts used: 4 pmol for GAPDH, 16 pmol for RAI1, and 4 pmol for BFP. This solution was added to cells, and then they were incubated overnight (>12 h) at 37°C.
Day 3: Probe solution was removed, and the cells resuspended with 500 µL of probe wash buffer, incubated for 10 min at 37°C, and then centrifuged for 5 min to remove the probe wash buffer. This step was repeated three additional times. Next, the pellet was resuspended with 500 µL of 5× SSCT, incubated for 5 min at room temperature, then centrifuged and re-suspended with 150 µL of amplification buffer and let sit for 30 minutes at room temperature. Then the amplification hairpins were separately prepared: 15 pmol of hairpin h1 and 15 pmol of hairpin h2 for each primary hairpin (6 total) by heating to 95°C for 90 seconds and then cooled to room temperature in a dark drawer for 30 min. The hairpins were then added to the sample and incubated overnight (>12 h) in the dark at room temperature.
Day 4: Cells were then centrifuged for 5 min and hairpin solution removed. The cells were then washed with 5× SSCT six times. Finally, cells were resuspended with flow buffer, filtered, and analyzed via flow cytometry as detailed previously.

Cell on a slide: mouse cortical neurons

Day 1: Growth media was aspirated from culture plates and cells were washed with PBST twice. 4% formaldehyde was then added to the cells and fixed for 1.5 hr at room temperature. Next, cells were washed 2x times with PBST and incubated 10min with 0.3% Triton-X-100. Samples were then washed with 2 × 300 µL of 2× SSC and pre-hybridized in 300 µL of probe hybridization buffer for 30 min at 37°C. Probe solution was then prepared similarly to the previous protocol, except amounts of probes were increased to: 8 pmol for GAPDH, 32 pmol for RAI1, and 10 pmol for BFP. They were then added to probe hybridization buffer, placed on the cells, and left overnight (>12 hrs).

Day 2: Excess probes were removed by washing 4 × 5 min with 300 µL of probe wash buffer at 37°C. Then, samples were washed with 2 × 5 min with 5× SSCT at room temperature, and then pre-amplified in 300 µL of amplification buffer for 30 min at room temperature. Hairpin amplification solution was prepared similarly to the previous protocol, and then added to the cells. Cells were then left at room temperature for 2 hours, and then washed 5 × 5 min with 300 µL of 5× SSCT at room temperature. Finally, 5× SSCT was aspirated and 300ul of ProLong® Gold Antifade Reagent with DAPI was added (Cell Signaling). Samples were then stored at 4°C and protected from light prior to imaging. Imaging took place over multiple days starting at one day post storage.

Microscopy experiments and analysis

All images were taken with the Inverted Zeiss LSM 780 multiphoton laser scanning confocal microscope. The following channels were used: AlexaFluor-488, AlexaFluor-546, AlexaFluor-647, and DAPI. Z-stack captures of 10-30 slices for each field of view were used to capture the entire volume of cells. Images for the dual AAV experiment were analyzed using FIJI/ImageJ: all Z-stack slices were combined using the MAX pixel intensity (z-project). GAPDH and DAPI channels remained untouched, while the Rai1 channel went through thresholding of 0.4% of intensity to MAX intensity for each well, and outlier pixels were removed (1 pixel size and 5 minimum intensity). Images were then converted into masked images (binary). Finally, the three channels were then combined, and the outline of each cell was manually drawn based on the combined GAPDH + DAPI signals. The percentage of positive RAI1 pixels in each cell was then automatically calculated and documented. Data was collected from two individual wells and combined. Images for the single AAV experiment were also analyzed using FIJI/ImageJ with a similar protocol. However, the Rai1 channel was threshold based off 0.4% of the MAX intensity of the no transduction well and applied to all conditions. Data across wells was not combined.

Analysis of predicted HI/TS genes

Since copy number variations are rare mutations, there is insufficient clinical data to understand dosage sensitivity for almost all genes. To address this problem, Collins et al. analyzed copy number variation data from 950,278 individuals and used machine learning to predict haploinsufficiency and triplosensitivity for all autosomal protein-coding genes within the human genome.[34] In this paper, we use data from Table S7: Haploinsufficiency and triplosensitivity predictions for all autosomal protein-coding genes. First, we screen for genes which have both a haploinsufficiency score (pHaplo) >= 0.86 and a triplosensitivity score (pTriplo) >= 0.94, indicating that the genes are predicted to be both haploinsufficient and triplosensitive (as defined by the authors). This resulted in a total of 915 genes after screening. Next, we used the Proteins REST API which provides data from UniProt to determine the protein sequence for each gene.[51] There were two genes with no return (AP000783.1, AC008443.1) which reduces the total number of dosage sensitive genes to 913. Lastly, we took the length of each protein sequence and multiplied by three to calculate the shortest possible gene length for each gene,

which is an underestimate of the final sequence which would be necessary for proper expression that would need to fit within an AAV.

Mathematical modeling for activation circuit simulations

To predict the behavior of the activation feedforward circuit, we construct an ordinary differential equation model assuming Michaelis-Menten kinetics, steady-state, and quasi-equilibrium. We incorporate interactions between dCas9 and the DNA, mRNA and protein production, first-order degradation of mRNA and proteins, and dCas9 cleavage by TEV.

We define the probability of active dCas9 binding to the target DNA (e.g. the *RAI1* gene) as:

$$Pb_{dCas9} = \frac{[dCas9]}{K_D + [dCas9]} \tag{1}$$

where K_D is the dCas9 dissociation constant and [*dCas9*] is the concentration of the active dCas9 protein. When we assume that cleaved dCas9 species competes with active dCas9 species to bind to the DNA, we add another term in the denominator to account for this competitive inhibition:

$$Pb_{dCas9} = \frac{[dCas9]}{K_D + [dCas9] + [dCas9_{cleaved}]} \tag{2}$$

Where [$dCas9_{cleaved}$] is the concentration of the cleaved dCas9 species.

Therefore, the change in corresponding target mRNA concentration is described by:

$$\frac{d[target\ mRNA]}{dt} = k_{on\ target} \cdot Pb_{dCas9} + k_{bac\ target} - k_{deg\ target\ mRNA} \cdot [target\ mRNA] \tag{3}$$

where $k_{bac\ target}$ is the background transcription rate of the target gene, $k_{on\ target}$ is the transcription rate when dCas9 is bound, and $k_{deg\ target\ mRNA}$ is the degradation rate of the target mRNA. The change in corresponding target protein concentration is described by:

$$\frac{d[target]}{dt} - k_{trans\ target} \cdot [target\ mRNA] - k_{deg\ target} \cdot [target] \tag{4}$$

where $k_{trans\ target}$ is the translation rate of the target protein and $k_{deg\ target}$ is the degradation rate of the target protein. The steady-state solutions for equation (3) and (4) are:

$$[target\ mRNA] = \frac{\left(k_{on\ target} \cdot Pb_{dCas9} + k_{bac\ target}\right)}{k_{deg\ target\ mRNA}} \tag{5}$$

$$[target] = \frac{k_{trans\ target} \cdot [target\ mRNA]}{k_{deg\ target}} \tag{6}$$

The dCas9 and TEV components are delivered to the cell such as in plasmid transfection and are therefore a function of dosage (DNA delivered). The TEV mRNA transcription rate can be represented by:

$$k_{on\ TEV\ mRNA} = a \cdot dosage \cdot DNA_{TEV} \tag{7}$$

where *a* is a constant representing the TEV transcription rate in units of concentration/(time*plasmid amount) (e.g. nM/h-ng plasmid), *dosage* is the amount of plasmid that is delivered to the cell, and DNA_{TEV} is the fraction of plasmid that encodes for TEV. The change in TEV mRNA concentration can therefore be described by:

$$\frac{d[TEV\ mRNA]}{dt} = k_{on\ TEV\ mRNA} - k_{deg\ TEV\ mRNA} \cdot [TEV\ mRNA] \tag{8}$$

Similarly, the dCas9 mRNA transcription rate is represented by:

$$k_{on\ dCas9\ mRNA} = a \cdot dosage \cdot DNA_{dCas9} \tag{9}$$

and the change in dCas9 mRNA concentration is described by:

$$\frac{d[dCas9\ mRNA]}{dt} = k_{on\ dCas9} - k_{deg\ dCas9\ mRNA} \cdot [dCas9\ mRNA] \tag{10}$$

The change in TEV protein concentration is described by:

$$\frac{d[TEV]}{dt} = k_{trans\ TEV} - k_{deg\ TEV} \cdot [TEV] \tag{11}$$

Lastly, the change in active dCas9 protein concentration is described by:

$$\frac{d[dCas9]}{dt} = k_{trans\ dCas9} \cdot [dCas9\ mRNA] - k_{deg\ dCas9} \cdot [dCas9] - k_{cut} \cdot [TEV] \cdot [dCas9] \tag{12}$$

where k_{cut} is the TEV k_{cat}/K_M, while the change in cleaved dCas9 protein concentration is described by:

$$\frac{d[Cas9_{cleaved}]}{dt} = k_{cut} \cdot [TEV] \cdot [dCas9] - k_{deg\ dCas9} \cdot [dCas9_{cleaved}] \tag{13}$$

The steady-state solutions for equations (8), (10), (11), (12), and (13) are respectively:

$$[TEV\ mRNA] = \frac{k_{on\ TEV}}{k_{deg\ TEV\ mRNA}} \tag{14}$$

$$[TEV] = \frac{k_{trans\ TEV} \cdot [TEV\ mRNA]}{k_{deg\ TEV}} \tag{15}$$

$$[dCas9\ mRNA] = \frac{k_{on\ dCas9}}{k_{deg\ dCas9\ mRNA}} \tag{16}$$

$$[dCas9] = \frac{k_{trans\ dCas9} \cdot [dCas9\ mRNA]}{k_{deg\ dCas9} + k_{cut} \cdot [TEV]} \tag{17}$$

$$[dCas9_{cleaved}] = \frac{k_{cut} \cdot [dCas9] \cdot [TEV]}{k_{deg\ dCas9}} \tag{18}$$

All numerical values, units, and references used for the parameters are found in Table S1.

Gating strategy for activation circuit titration

We observe a non-monotonic trend at high transfection levels for the running means of the activation circuit titration (SFig. 1A). Measuring the average GFP fluorescence of all transfected cells masks this non-monotonic effect (SFig. 1B). Since this non-monotonic effect biases the average GFP fluorescence of all transfected cells, we present the activation circuit titration in **Fig. 1F** as the average of transfected cells with an mCherry fluorescence below 10^7.

Increasing TEV sensitivity of the activation circuit

Another method of tuning the circuit is to change the efficiency of the TEV cut site between dCas9 and the transcriptional activator. An easy way to increase the efficiency is to use tandem TEV cut sites. Thus, we created a construct that had two TEV cut sites and compared it to our original construct which contains one (SFig. 1C). The double TEV cut site construct was much more sensitive to TEV, requiring much less to repress gene activation. We note that the double TEV cut site construct also has lower gene activation ability, possibly due to the transcriptional activator being further away from the DNA due to the longer linker.

Engineering a TEV cleavable Cas13

Mathematical modeling for repression circuit simulations

To predict the behavior of the repression feedforward circuit, we construct an ordinary differential equation model assuming Michaelis-Menten kinetics, steady-state, and quasi-equilibrium. We incorporate interactions between Cas13 and the target mRNA, mRNA and protein production, first-order degradation of mRNA and proteins, and Cas13 cleavage by TEV. Unfortunately, there is little kinetic data for CasRx in contrast to TEV. Furthermore, much of the kinetic data available measures off-target mRNA cleavage rather than on-target mRNA

cleavage. Therefore, we also assume that k_{cat}/K_M for Cas13 is the same as TEV, though this is likely not the case. The change in corresponding target mRNA concentration is described by:

$$\frac{d[target\ mRNA]}{dt} = k_{bac\ target} - k_{cut\ Cas13} \cdot [Cas13] \cdot [target\ mRNA] - k_{deg\ target\ mRNA} \cdot [target\ mRNA] \tag{19}$$

where $k_{bac\ target}$ is the background transcription rate of the target gene, $k_{cut\ Cas13}$ is the k_{cut}/K_M for Cas13, and $k_{deg\ target\ mRNA}$ is the degradation rate of the target mRNA. The change in corresponding target protein concentration is described by:

$$\frac{d[target]}{dt} = k_{trans\ target} \cdot [target\ mRNA] - k_{deg\ target} \cdot [target] \tag{20}$$

where $k_{trans\ target}$ is the translation rate of the target protein and $k_{deg\ target}$ is the degradation rate of the target protein. The steady-state solutions for equation (19) and (20) are:

$$[target\ mRNA] = \frac{k_{bac\ target}}{k_{cut\ Cas13} \cdot [Cas13] + k_{deg\ target\ mRNA}} \tag{21}$$

$$[target] = \frac{k_{trans\ target} \cdot [target\ mRNA]}{k_{deg\ target}} \tag{22}$$

The Cas13 and TEV components are delivered to the cell such as in plasmid transfection and are therefore a function of dosage (DNA delivered). The TEV mRNA transcription rate can be represented by:

$$k_{on\ TEV\ mRNA} = a \cdot dosage \cdot DNA_{TEV} \tag{23}$$

where *a* is a constant representing the TEV transcription rate in units of concentration/(time*plasmid amount) (e.g. nM/h-ng plasmid), *dosage* is the amount of plasmid that is delivered to the cell, and DNA_{TEV} is the fraction of plasmid that encodes for TEV. The change in TEV mRNA concentration can therefore be described by:

$$\frac{d[TEV\ mRNA]}{dt} = k_{on\ TEV\ mRNA} - k_{deg\ TEV\ mRNA} \cdot [TEV\ mRNA] \tag{24}$$

Similarly, the Cas13 mRNA transcription rate is represented by:

$$k_{on\ Cas13\ mRNA} = a \cdot dosage \cdot DNA_{Cas13} \tag{25}$$

and the change in dCas9 mRNA concentration is described by:

$$\frac{d[Cas13\ mRNA]}{dt} = k_{on\ Cas13} - k_{deg\ Cas13\ mRNA} \cdot [Cas13\ mRNA] \tag{26}$$

The change in TEV protein concentration is described by:

$$\frac{d[TEV]}{dt} = k_{trans\ TEV} - k_{deg\ TEV} \cdot [TEV] \tag{27}$$

Lastly, the change in active dCas9 protein concentration is described by:

$$\frac{d[Cas13]}{dt} = k_{trans\ Cas13} \cdot [Cas13\ mRNA] - k_{deg\ Cas13} \cdot [dCas9] - k_{cut\ TEV} \cdot [TEV] \cdot [Cas13] \tag{28}$$

where $k_{cut\ TEV}$ is the TEV k_{cat}/K_M.

The steady-state solutions for equations (24), (26), (27), and (28) are respectively:

$$[TEV\ mRNA] = \frac{k_{on\ TEV}}{k_{deg\ TEV\ mRNA}} \tag{29}$$

$$[TEV] = \frac{k_{trans\ TEV} \cdot [TEV\ mRNA]}{k_{deg\ TEV}} \tag{30}$$

$$[Cas13\ mRNA] = \frac{k_{on\ Cas13}}{k_{deg\ Cas13\ mRNA}} \tag{31}$$

$$[Cas13] = \frac{k_{trans\ Cas13} \cdot [Cas13\ mRNA]}{k_{cut\ TEV} \cdot [TEV] + k_{deg\ Cas13}} \tag{32}$$

All numerical values, units, and references used for the parameters are found in Table S1.

Calculating the plasmid transcription rate for the simulations

To estimate the value of the plasmid transcription ate *a*, as mentioned in equation (7), (9), (23), and (25), we use experimental data and data reported for GFP fluorescence in the supplementary information of a paper previously published by the Gao lab.[52] We conducted an experiment where 10 ng of CMVTO-GFP was transfected for a single 24-well of HEK293 cells and measured an average GFP fluorescence of 1.3*10^6 A.U. From Fig. S2A and S2C from Kaseniit *et al*., we estimate that 300 copies of GFP mRNA corresponds to a measured fluorescence of 7*10^5 A.U. (we multiply the reported value by 100 due to differences in normalization between analysis software). 300 copies of mRNA is 0.5 nM of mRNA using Avogadro's number and an estimated cell volume of 1 pL. Assuming a linear relationship between average GFP fluorescence and ng of DNA transfected, we would estimate that an average GFP fluorescence of $7*10^5$ would correspond to 5.38 ng of plasmid transfected. Since these measurements were taken at steady state, we calculate *a* using the following equation set equal to zero:

$$\frac{d[plasmid\ mRNA]}{dt} = a \cdot (ng\ plasmid) - k_{deg}[plasmid\ mRNA] = 0 \tag{33}$$

$$a = \frac{k_{deg}[plasmid\ mRNA]}{[plasmid]} \tag{34}$$

We estimate the ng plasmid per cell by dividing 5.38 ng by $0.24*10^6$, the number of cells within a confluent well of a 24-well plate,[53] to determine (*ng plasmid*). We previously calculated [*plasmid mRNA*] to be 0.5 nM. Lastly, we use an estimate for the median mRNA degradation rate (Table S1). We then solve for *a* resulting in $1.71*10^3$ nM/(h-ng plasmid).

References

1. Wan, Y., Cohen, J., Szenk, M., Farquhar, K.S., Coraci, D., Krzysztoń, R., Azukas, J., Van Nest, N., Smashnov, A., Chern, Y.-J., et al. (2023). Nonmonotone invasion landscape by noise-aware control of metastasis activator levels. Nat. Chem. Biol. *19*, 887–899. 10.1038/s41589-023-01344-z.

2. Peier, A.M., McIlwain, K.L., Kenneson, A., Warren, S.T., Paylor, R., and Nelson, D.L. (2000). (Over)correction of FMR1 deficiency with YAC transgenics: behavioral and physical features. Hum. Mol. Genet. *9*, 1145–1159. 10.1093/hmg/9.8.1145.

3. Huichalaf, C., Perfitt, T.L., Kuperman, A., Gooch, R., Kovi, R.C., Brenneman, K.A., Chen, X., Hirenallur-Shanthappa, D., Ma, T., Assaf, B.T., et al. (2022). In vivo overexpression of frataxin causes toxicity mediated by iron-sulfur cluster deficiency. Mol. Ther. Methods Clin. Dev. *24*, 367–378. 10.1016/j.omtm.2022.02.002.

4. Belbellaa, B., Reutenauer, L., Messaddeq, N., Monassier, L., and Puccio, H. (2020). High levels of frataxin overexpression lead to mitochondrial and cardiac toxicity in mouse models. Mol. Ther. Methods Clin. Dev. *19*, 120–138. 10.1016/j.omtm.2020.08.018.

5. Tamura, S., Nelson, A.D., Spratt, P.W.E., Hamada, E.C., Zhou, X., Kyoung, H., Li, Z., Arnould, C., Barskyi, V., Krupkin, B., et al. (2025). CRISPR activation for SCN2A-related neurodevelopmental disorders. Nature. 10.1038/s41586-025-09522-w.

6. Collins, B.E., and Neul, J.L. (2022). Rett syndrome and MECP2 duplication syndrome: disorders of mecp2 dosage. Neuropsychiatr. Dis. Treat. *18*, 2813–2835. 10.2147/NDT.S371483.

7. Javed, S., Selliah, T., Lee, Y.-J., and Huang, W.-H. (2020). Dosage-sensitive genes in autism spectrum disorders: From neurobiology to therapy. Neurosci. Biobehav. Rev. *118*, 538–567. 10.1016/j.neubiorev.2020.08.009.

8. Smith, A.C., McGavran, L., Robinson, J., Waldstein, G., Macfarlane, J., Zonona, J., Reiss, J., Lahr, M., Allen, L., and Magenis, E. (1986). Interstitial deletion of (17)(p11.2p11.2) in nine patients. Am. J. Med. Genet. *24*, 393–414. 10.1002/ajmg.1320240303.

9. Slager, R.E., Newton, T.L., Vlangos, C.N., Finucane, B., and Elsea, S.H. (2003). Mutations in RAI1 associated with Smith-Magenis syndrome. Nat. Genet. *33*, 466–468. 10.1038/ng1126.

10. Potocki, L., Bi, W., Treadwell-Deering, D., Carvalho, C.M.B., Eifert, A., Friedman, E.M., Glaze, D., Krull, K., Lee, J.A., Lewis, R.A., et al. (2007). Characterization of Potocki-Lupski syndrome (dup(17)(p11.2p11.2)) and delineation of a dosage-sensitive critical interval that can convey an autism phenotype. Am. J. Hum. Genet. *80*, 633–649. 10.1086/512864.

11. Carmona-Mora, P., and Walz, K. (2010). Retinoic acid induced 1, RAI1: A dosage sensitive gene related to neurobehavioral alterations including autistic behavior. Curr. Genomics *11*, 607–617. 10.2174/138920210793360952.

12. Huang, W.-H., Guenthner, C.J., Xu, J., Nguyen, T., Schwarz, L.A., Wilkinson, A.W., Gozani, O., Chang, H.Y., Shamloo, M., and Luo, L. (2016). Molecular and Neural Functions of Rai1, the Causal Gene for Smith-Magenis Syndrome. Neuron *92*, 392–406. 10.1016/j.neuron.2016.09.019.

13. Rinaldi, B., Villa, R., Sironi, A., Garavelli, L., Finelli, P., and Bedeschi, M.F. (2022). Smith-Magenis Syndrome-Clinical Review, Biological Background and Related Disorders. Genes *13*. 10.3390/genes13020335.

14. Chang, H.-C., Lee, Y.-J., Javed, S., Haque, M., Chang, Y.-T., Lin, Y.C., Oram, C., and Huang, W.-H. (2023). rAAV-CRISPRa therapy corrects Rai1 haploinsufficiency and rescues selective disease features in Smith-Magenis syndrome mice. J. Biol. Chem. *299*, 102728. 10.1016/j.jbc.2022.102728.

15. Zhu, G., Zhou, X., Wen, M., Qiao, J., Li, G., and Yao, Y. (2024). CRISPR-Cas13: Pioneering RNA Editing for Nucleic Acid Therapeutics. BioDesign Research *6*, 0041. 10.34133/bdr.0041.

16. Ling, Q., Herstine, J.A., Bradbury, A., and Gray, S.J. (2023). AAV-based in vivo gene therapy for neurological disorders. Nat. Rev. Drug Discov. *22*, 789–806. 10.1038/s41573-023-00766-7.

17. Fong, S., Yates, B., Sihn, C.-R., Mattis, A.N., Mitchell, N., Liu, S., Russell, C.B., Kim, B., Lawal, A., Rangarajan, S., et al. (2022). Interindividual variability in transgene mRNA and protein production following adeno-associated virus gene therapy for hemophilia A. Nat. Med. *28*, 789–797. 10.1038/s41591-022-01751-0.

18. Puzzo, F., and Kay, M.A. (2025). The deLIVERed promises of gene therapy: Past, present, and future of liver-directed gene therapy. Mol. Ther. *33*, 1966–1987. 10.1016/j.ymthe.2025.03.041.

19. Reeves, G.T. (2019). The engineering principles of combining a transcriptional incoherent feedforward loop with negative feedback. J. Biol. Eng. *13*, 62. 10.1186/s13036-019-0190-3.

20. Ma, W., Trusina, A., El-Samad, H., Lim, W.A., and Tang, C. (2009). Defining network topologies that can achieve biochemical adaptation. Cell *138*, 760–773. 10.1016/j.cell.2009.06.013.

21. Strovas, T.J., Rosenberg, A.B., Kuypers, B.E., Muscat, R.A., and Seelig, G. (2014). MicroRNA-based single-gene circuits buffer protein synthesis rates against perturbations. ACS Synth. Biol. *3*, 324–331. 10.1021/sb4001867.

22. Segall-Shapiro, T.H., Sontag, E.D., and Voigt, C.A. (2018). Engineered promoters enable constant gene expression at any copy number in bacteria. Nat. Biotechnol. *36*, 352–358. 10.1038/nbt.4111.

23. Yang, J., Lee, J., Land, M.A., Lai, S., Igoshin, O.A., and St-Pierre, F. (2021). A synthetic circuit for buffering gene dosage variation between individual mammalian cells. Nat. Commun. *12*, 4132. 10.1038/s41467-021-23889-0.

24. Mallozzi, A., Fusco, V., Ragazzini, F., and di Bernardo, D. (2024). The CRISPRaTOR: a biomolecular circuit for Automatic Gene Regulation in Mammalian Cells with CRISPR technology. BioRxiv. 10.1101/2024.03.30.587417.

25. Love, K.S., Johnstone, C.P., Peterman, E.L., Gaglione, S., and Galloway, K.E. (2024). Model-guided design of microRNA-based gene circuits supports precise dosage of transgenic cargoes into diverse primary cells. BioRxiv. 10.1101/2024.06.25.600629.

26. Shimoga, V., White, J.T., Li, Y., Sontag, E., and Bleris, L. (2013). Synthetic mammalian transgene negative autoregulation. Mol. Syst. Biol. *9*, 670. 10.1038/msb.2013.27.

27. Du, R., Flynn, M.J., Honsa, M., Jungmann, R., and Elowitz, M.B. (2024). miRNA circuit modules for precise, tunable control of gene expression. BioRxiv. 10.1101/2024.03.12.583048.

28. Jones, R.D., Qian, Y., Siciliano, V., DiAndreth, B., Huh, J., Weiss, R., and Del Vecchio, D. (2020). An endoribonuclease-based feedforward controller for decoupling resource-limited genetic modules in mammalian cells. Nat. Commun. *11*, 5690. 10.1038/s41467-020-19126-9.

29. Flynn, M.J., Mayfield, A.M.H., Du, R., Gradinaru, V., and Elowitz, M.B. (2024). Synthetic dosage-compensating miRNA circuits allow precision gene therapy for Rett syndrome. BioRxiv. 10.1101/2024.03.13.584179.

30. Love, K.S., Johnstone, C.P., Peterman, E.L., Gaglione, S., Birnbaum, M.E., and Galloway, K.E. (2025). Model-guided design of microRNA-based gene circuits supports precise dosage of transgenic cargoes into diverse primary cells. Cell Syst., 101269. 10.1016/j.cels.2025.101269.

31. Wang, J., Ding, Y., Chong, K., Cui, M., Cao, Z., Tang, C., Tian, Z., Hu, Y., Zhao, Y., and Jiang, S. (2024). Recent Advances in Lipid Nanoparticles and Their Safety Concerns for mRNA Delivery. Vaccines (Basel) *12*. 10.3390/vaccines12101148.

32. Gao, X.J., Chong, L.S., Kim, M.S., and Elowitz, M.B. (2018). Programmable protein circuits in living cells. Science *361*, 1252–1258. 10.1126/science.aat5062.

33. Fink, T., Lonzarić, J., Praznik, A., Plaper, T., Merljak, E., Leben, K., Jerala, N., Lebar, T., Strmšek, Ž., Lapenta, F., et al. (2019). Design of fast proteolysis-based signaling and logic circuits in mammalian cells. Nat. Chem. Biol. *15*, 115–122. 10.1038/s41589-018-0181-6.

34. Collins, R.L., Glessner, J.T., Porcu, E., Lepamets, M., Brandon, R., Lauricella, C., Han, L., Morley, T., Niestroj, L.-M., Ulirsch, J., et al. (2022). A cross-disorder dosage sensitivity map of the human genome. Cell *185*, 3041-3055.e25. 10.1016/j.cell.2022.06.036.

35. Konermann, S., Lotfy, P., Brideau, N.J., Oki, J., Shokhirev, M.N., and Hsu, P.D. (2018). Transcriptome Engineering with RNA-Targeting Type VI-D CRISPR Effectors. Cell *173*, 665-676.e14. 10.1016/j.cell.2018.02.033.

36. Cohen, R.N., van der Aa, M.A.E.M., Macaraeg, N., Lee, A.P., and Szoka, F.C. (2009). Quantification of plasmid DNA copies in the nucleus after lipoplex and polyplex transfection. J. Control. Release *135*, 166–174. 10.1016/j.jconrel.2008.12.016.

37. Tycko, J., Van, M.V., Aradhana, DelRosso, N., Ye, H., Yao, D., Valbuena, R., Vaughan-Jackson, A., Xu, X., Ludwig, C., et al. (2024). Development of compact transcriptional effectors using high-throughput measurements in diverse contexts. Nat. Biotechnol. 10.1038/s41587-024-02442-6.

38. Wehr, M.C., Laage, R., Bolz, U., Fischer, T.M., Grünewald, S., Scheek, S., Bach, A., Nave, K.-A., and Rossner, M.J. (2006). Monitoring regulated protein-protein interactions using split TEV. Nat. Methods *3*, 985–993. 10.1038/nmeth967.

39. Cory, T.J., Mu, Y., Gong, Y., Kodidela, S., and Kumar, S. (2018). Sofosbuvir + velpatasvir + voxilaprevir for the treatment of hepatitis C infection. Expert Opin. Pharmacother. *19*, 749–757. 10.1080/14656566.2018.1459567.

40. Gupta, R., Ghosh, A., Chakravarti, R., Singh, R., Ravichandiran, V., Swarnakar, S., and Ghosh, D. (2022). Cas13d: A new molecular scissor for transcriptome engineering. Front. Cell Dev. Biol. *10*, 866800. 10.3389/fcell.2022.866800.

41. Shi, P., Murphy, M.R., Aparicio, A.O., Kesner, J.S., Fang, Z., Chen, Z., Trehan, A., Guo, Y., and Wu, X. (2023). Collateral activity of the CRISPR/RfxCas13d system in human cells. Commun. Biol. *6*, 334. 10.1038/s42003-023-04708-2.

42. Varshavsky, A. (2011). The N-end rule pathway and regulation by proteolysis. Protein Sci. *20*, 1298–1345. 10.1002/pro.666.

43. Tong, H., Huang, J., Xiao, Q., He, B., Dong, X., Liu, Y., Yang, X., Han, D., Wang, Z., Wang, X., et al. (2023). High-fidelity Cas13 variants for targeted RNA degradation with minimal collateral effects. Nat. Biotechnol. *41*, 108–119. 10.1038/s41587-022-01419-7.

44. Choi, H.M.T., Schwarzkopf, M., Fornace, M.E., Acharya, A., Artavanis, G., Stegmaier, J., Cunha, A., and Pierce, N.A. (2018). Third-generation in situ hybridization chain reaction: multiplexed, quantitative, sensitive, versatile, robust. Development *145*. 10.1242/dev.165753.

45. Carmona-Mora, P., Canales, C.P., Cao, L., Perez, I.C., Srivastava, A.K., Young, J.I., and Walz, K. (2012). RAI1 transcription factor activity is impaired in mutants associated with Smith-Magenis Syndrome. PLoS ONE *7*, e45155. 10.1371/journal.pone.0045155.

46. Lacaria, M., Gu, W., and Lupski, J.R. (2013). Circadian abnormalities in mouse models of Smith-Magenis syndrome: evidence for involvement of RAI1. Am. J. Med. Genet. A *161A*, 1561–1568. 10.1002/ajmg.a.35941.

47. Huang, W.-H., Wang, D.C., Allen, W.E., Klope, M., Hu, H., Shamloo, M., and Luo, L. (2018). Early adolescent Rai1 reactivation reverses transcriptional and social interaction deficits in a mouse model of Smith-Magenis syndrome. Proc Natl Acad Sci USA *115*, 10744–10749. 10.1073/pnas.1806796115.

48. Wang, J., Lin, J., Chen, Y., Liu, J., Zheng, Q., Deng, M., Wang, R., Zhang, Y., Feng, S., Xu, Z., et al. (2023). An ultra-compact promoter drives widespread neuronal expression in mouse and monkey brains. Cell Rep. *42*, 113348. 10.1016/j.celrep.2023.113348.

49. Hsu, P.D., Scott, D.A., Weinstein, J.A., Ran, F.A., Konermann, S., Agarwala, V., Li, Y., Fine, E.J., Wu, X., Shalem, O., et al. (2013). DNA targeting specificity of RNA-guided Cas9 nucleases. Nat. Biotechnol. *31*, 827–832. 10.1038/nbt.2647.

50. Kemaladewi, D.U., Bassi, P.S., Erwood, S., Al-Basha, D., Gawlik, K.I., Lindsay, K., Hyatt, E., Kember, R., Place, K.M., Marks, R.M., et al. (2019). A mutation-independent approach for muscular dystrophy via upregulation of a modifier gene. Nature *572*, 125–130. 10.1038/s41586-019-1430-x.

51. Nightingale, A., Antunes, R., Alpi, E., Bursteinas, B., Gonzales, L., Liu, W., Luo, J., Qi, G., Turner, E., and Martin, M. (2017). The Proteins API: accessing key integrated protein and genome information. Nucleic Acids Res. *45*, W539–W544. 10.1093/nar/gkx237.

52. Kaseniit, K.E., Katz, N., Kolber, N.S., Call, C.C., Wengier, D.L., Cody, W.B., Sattely, E.S., and Gao, X.J. (2023). Modular, programmable RNA sensing using ADAR editing in living cells. Nat. Biotechnol. *41*, 482–487. 10.1038/s41587-022-01493-x.

53. Useful Numbers for Cell Culture | Thermo Fisher Scientific - US https://www.thermofisher.com/us/en/home/references/gibco-cell-culture-basics/cell-culture-protocols/cell-culture-useful-numbers.html. Sciwheel inserting bibliography...